

4-2022

Modeling and Analyses of Mechanisms Underlying Network Synaptic Dynamics in Two Neural Circuits

Linda Ma
William & Mary

Follow this and additional works at: <https://scholarworks.wm.edu/honorsthesis>



Part of the [Applied Mathematics Commons](#), and the [Computational Neuroscience Commons](#)

Recommended Citation

Ma, Linda, "Modeling and Analyses of Mechanisms Underlying Network Synaptic Dynamics in Two Neural Circuits" (2022). *Undergraduate Honors Theses*. William & Mary. Paper 1750.
<https://scholarworks.wm.edu/honorsthesis/1750>

This Honors Thesis -- Open Access is brought to you for free and open access by the Theses, Dissertations, & Master Projects at W&M ScholarWorks. It has been accepted for inclusion in Undergraduate Honors Theses by an authorized administrator of W&M ScholarWorks. For more information, please contact scholarworks@wm.edu.

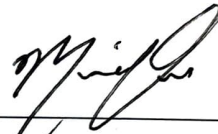
Modeling and analyses of mechanisms underlying network synaptic
dynamics in two neural circuits

A thesis submitted in partial fulfillment of the requirement
for the degree of Bachelor of Science in Mathematics from William & Mary

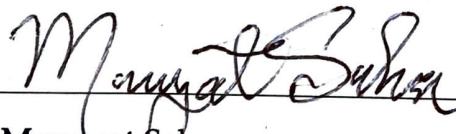
by

Linda Ma

Accepted for: Honors



Dr. Mainak Patel, advisor



Dr. Margaret Saha



Dr. Leah Shaw

College of William & Mary

April 26, 2022

Abstract

In systems neuroscience, circuit models of cortical structures can be used to deconstruct mechanisms responsible for spike patterns that generate a variety of behaviors observed in the brain. In particular, mathematical simulations of these circuits can replicate complex dynamical behaviors that mirror not only macroscopically patterns observed in the brain, but also a significant amount of experimentally characterized minutiae. These models are capable of analyzing neural mechanisms by explicitly deconstructing connectivities between populations of neurons in ways that tend to be empirically inaccessible. This work presents two such models; one in the rat somatosensory barrel cortex, responsible for processing sensory information from whiskers, and one in the CA3 subfield of the hippocampus, responsible for, among other higher brain functions, memory storage and retrieval. In the former we model the generation of multiwhisker receptive fields by lateral (as opposed to feedforward) synaptic connections in layer IV of the barrel cortex, and show that this hypothesis can capture a range of experimentally characterized responses. In the latter we study the generation of gamma frequency oscillations in the CA3, in particular examining the shift between two network regimes of oscillations upon activation of NMDA receptors. These models are constructed as networks of coupled ordinary differential equations representing integrate and fire neurons, and simulations are computed via numerical integration by the forward Euler method.

Contents

Abstract	i
1 Introduction	1
2 Multiwhisker RFs in the Barrel Cortex	6
2.1 Introduction	7
2.2 Results	12
2.2.1 Single Whisker Deflections	13
2.2.2 Paired Whisker Deflections	17
2.2.3 Three Barrel Model	23
2.3 Discussion	27
2.4 Methods	29
2.4.1 Model Connectivity	30
2.4.2 Model Equations	32
2.4.3 Stimulus Modeling	34
2.4.4 Simulation and Data Analysis	34
3 γ Frequency Oscillations in the CA3	37
3.1 Introduction	38
3.2 Results	40
3.2.1 Network Behavior Without NMDA	41
3.2.2 Network Behavior With NMDA	46
3.2.3 Mechanism of Gamma Oscillations	51
3.3 Discussion	56
3.3.1 Model Parameters	57
3.3.2 Other Models	57
3.4 Methods	58

3.4.1	Model Equations	59
3.4.2	Parameters	60
3.4.3	Data Analysis	61
4	Discussion	63
	Acknowledgments	65
	Bibliography	66

Chapter 1

Introduction

Neural circuits form the basis for many cortical functions, and studying the computations they carry out allows us to examine such functions with a fairly high degree of complexity, providing explanations for different mechanisms that generate the overall network behavior. Construction of these circuits as networks using modeling methods allows explicit study of synaptic connectivity between neurons in the network, allowing us to isolate the effects yielded by specific currents or populations of neurons. Such models are particularly useful for characterizing physiological behaviors that lack experimentally testable explanations. In this work, we see two examples of such circuits that can be studied and analyzed using computational models, offering insight into the mechanisms behind the functions they are responsible for.

The first of these models studies the generation of spike patterns from sensory whisker inputs to the rat barrel cortex. Sensory information in the barrel cortex is propagated through a circuit composed of thalamocortical neurons, regular-spiking excitatory cells and fast-spiking inhibitory cells. We focus specifically on layer IV, main target of sensory info from thalamocortical (TC) cells. The circuit uses a phase-delayed network architecture, in which input from fast-spiking (FS) neurons modulates excitatory currents through feedforward inhibition, by synapsing simultaneously onto themselves and regular-spiking (RS) neurons before excitatory RS currents have a chance to propagate. Upon being stimulated, specific whiskers transmit an initial wave of excitation to a population of direction selective TC cells, which then synapse onto a corresponding specific barrel. A subset of cells within each barrel have multiwhisker receptive fields; that is, they encode signals in response to deflection of a whisker adjacent (AW) to their principal whisker (PW), independent of stimulation of their PW. There are two mechanisms speculated to yield these AW deflection responses; empirical studies show conflicting results on whether these are generated by lateral or feedforward networks. We study the former, which

suggests that signals from AWs synapse onto their corresponding barrel, and it is within the cortical layers that responses propagate laterally between barrels. We construct a network model of a single barrel within the barrel cortex to simulate experimental conditions from the literature to check baseline responses for PW deflections, then model neighboring barrels, connected through lateral synapses, to examine responses such as direction tuning, suppression/facilitation, and GABA blockage.

The second model studies oscillations in the CA3 region of the hippocampus, specifically the effect of NMDA receptor activation on triggering a switch between two network regimes (excitation-inhibition 'E-I' and inhibition-inhibition 'I-I') that generate gamma frequency oscillations. These oscillations occur at frequency bands spanning 30 – 120 Hz, and are observed to be activated by populations of excitatory pyramidal neurons and inhibitory interneurons firing in synchrony, mediated by AMPA and GABA currents in the CA3. Genetic knockout of delta-GABA receptors in the CA3 subfield of the hippocampus reveals an underlying NMDA current that modulates oscillation frequency, which increases base oscillation frequencies from 40 Hz to ~ 60 Hz and yields decreased phase differences between PN and IN peaks. This is hypothesized to occur due to a shift from the 'E-I' to the 'I-I' mechanism as the source of these oscillations. In the intact 'E-I' network, interneurons are driven by excitation from pyramidal neurons, and subsequently shut down the pyramidal neurons in a periodic pattern, whereas in the NMDA mediated 'I-I' network, inhibitory interneurons are sustained by NMDA currents and can oscillate independent of fast excitatory synapses. We develop a network model of the CA3, first replicating baseline 40 Hz oscillations, and then introducing NMDA receptors to examine changes in oscillation frequency and synchrony between populations of PNs and INs with our computational model, empirical results suggesting a shift in oscillation mechanism.

Neurons communicate with each other via action potentials, electrical impulses that they output when sufficiently excited, and networks of these neurons can be thought of as a dynamical system. Both of these studies use networks of the leaky integrate-and-fire model (LIF) of a neuron, a system composed of coupled ordinary differential equations, each of which describe the spiking dynamics of a single neuron. A neuron grows excited as its voltage increases relative to its environment, and fires an action potential, or a spike, once it receives enough excitatory current from neurons that synapse onto it. Once a neuron spikes, it outputs either an excitatory or inhibitory current to other neurons in the network. The IF model treats a neuron as an electrical

circuit, and uses Ohm's law

$$V = IR$$

to describe the interplay of voltage V , current I , and resistance R that determines the flow of charged ions through receptors in a neuron. The voltage of a neuron is described in terms of membrane potential, the difference between the charge of a neuron and the extracellular environment surrounding it. Each receptor gates a particular type of ion, and is associated with a different type of current; this allows us to partition excitatory and inhibitory current into their own terms. Conventionally, we use conductance $g = \frac{1}{R}$, the inverse of resistance, to describe how permeable the membrane is to the flow of current. Thus,

$$I = g\Delta V = g_n(V - E_n)$$

denotes the current reaching a neuron from a particular type of receptor gating an ion n as the neuron's membrane potential varies over time. Each presynaptic spike using this receptor leads to a jump in conductance g_n , and increases in g_n represent ion channels of n opening. Each ion has its own default charge and concentration/electrical gradient when a neuron is at rest, and as channels open, chemical and electrical concentration gradients equilibrate by letting n out or in. E_n is equilibrium potential of n , at which point the electrical gradient exactly balances out concentration gradient and the flow stops. Thus $V - E_n$ measures potential difference driving the current; as V approaches E_n , flow of current decreases. E_n is above resting potential for excitatory currents and below resting potential for inhibitory currents; thus the magnitude of $V - E_n$ determines the driving force and the sign determines the direction of ion flow.

To determine overall change in membrane potential due to flow of current, we sum the current from each type of receptor, as well as external current and activity of leak channels. The general form of a single I&F neuron in a conductance-based model is

$$\dot{V} = I_{\text{ext}} - \sum_i^n g_{n_i}(V - V_{n_i}) - g_L(V - V_L)$$

where \dot{V} represents how membrane potential changes over time. Each of these is coupled to other neurons in the network by the g_n terms, which record inputs from neurons presynaptic to this particular neuron. Once V reaches a threshold, set to 1 in our non-dimensionalized model,

the neuron spikes, and membrane potential resets to its natural resting state, $V_{\text{rest}} = 0$. To simulate a refractory period, where a neuron is briefly incapable of spiking again after it fires, we fix V at 0 for 2ms after every spike. For each r^{th} presynaptic spike occurs at time t_r , the conductance $g(t)$ induced in the neuron at time t is given by the following:

$$i_r(t) = \begin{cases} 0 & t < t_r + l, \\ Ae^{-\frac{t-(t_r+l)}{\tau}} & \geq t_r + l. \end{cases}$$

$$g(t) = \sum_{r=1}^k i_r(t),$$

where the latency l denotes how long a signal takes to reach the postsynaptic neuron after presynaptic neuron fires; inputs generates 0 conductance until the delay period ends, then causes a conductance change described by $i_r(t)$ as a function of amplitude A , the strength of the input, and decay rate τ , how long current lingers in neuron before decaying by $\frac{2}{3}$ of its value. k denotes the total number of presynaptic spikes onto the neuron, and the total current reaching the postsynaptic neuron at any given time is the sum of all inputs from presynaptic neurons that contact it at time t .

I_{ext} denotes an external current that is not intrinsic to the dynamics of the network; these currents usually supply initial excitation to the network from an outside source, representing some kind of external stimulus, that triggers the network to react and encode that stimulus. The 'leaky' part of the LIF neuron comes from the g_L term, which represents the tendency of the neuron to reset to its natural resting state, V_{rest} as leak channels allow excitation to naturally decay over time. g_L are constant values representing conductance of leak channels (which are constitutively open).

Recall that current reaching the neuron through the receptors for ion n is a function of conductance g and driving force $V - E_n$, which decreases as electrical/chemical imbalance is equalized. We can further simplify this model by assuming that V is always reasonably far enough from the equilibrium potential of any n in the system, and thus driving force does not change dramatically. Then, rather than having presynaptic spikes change the value of g , we can have values of i jump directly. This gives us

$$\frac{dV}{dt} = -g(V - V_{\text{rest}}) + I(t),$$

$$I(t) = \sum_{r=1}^k i_r(t),$$

with i defined as above. We can generally partition current-based IF neuron equations into two terms; $g(V - V_{rest})$, which represents loss of excitation through leak channels, and $I(t)$, which governs all incoming currents from presynaptic neurons. In this model we manually set excitatory I as positive and inhibitory I as negative.

Chapter 2

Multiwhisker RFs in the Barrel Cortex¹

Abstract

While cells within barrel cortex respond primarily to deflections of their principal whisker (PW), they also exhibit responses to non-principal, or adjacent, whiskers (AWs), albeit responses with diminished amplitudes and longer latencies. The origin of multiwhisker receptive fields of barrel cells remains a point of controversy within the experimental literature, with three contending possibilities: *(i)* barrel cells inherit their AW responses from the AW responses of thalamocortical (TC) cells within their aligned barreloid; *(ii)* the axons of TC cells within a barreloid ramify to innervate multiple barrels, rather than only terminating within their aligned barrel; *(iii)* lateral intracortical transmission between barrels conveys AW responsivity to barrel cells. In this work, we develop a detailed, biologically plausible model of multiple barrels in order to examine possibility *(iii)*; in order to isolate the dynamics that possibility *(iii)* entails, we incorporate lateral connections between barrels while assuming that TC cells respond only to their PW and that TC cell axons are confined to their home barrel. We show that our model is capable of capturing a broad swath of experimental observations on multiwhisker receptive field dynamics within barrels, and we compare and contrast the dynamics of this model with model dynamics from prior work in which employ a similar general modeling strategy to examine possibility *(i)*.

¹Ma, L. & Patel, M. (2021). A Model of Lateral Interactions as the Origin of Multiwhisker Receptive Fields in Rat Barrel Cortex. *Journal of Computational Neuroscience*, <https://doi.org/10.1007/s10827-021-00804-6>. L.M. implemented the model, analyzed the data, and drafted the manuscript. M.P designed the study and revised the manuscript.

2.1 Introduction

The rat barrel cortex is organized in a functionally segregated manner by whisker, with each whisker corresponding to a modular pathway beginning at somatosensory receptors on the mystacial pad and traversing through the thalamus up to the barrel cortex. Within the thalamus, input from a particular whisker is received by ~ 250 thalamocortical (TC) cells within a dedicated thalamic barreloid, which in turn excite two types of cells within layer IV of a dedicated cortical barrel – < 400 inhibitory fast-spiking (FS) cells and ~ 3600 excitatory regular-spiking (RS) cells. FS cells within a barrel, in turn, supply potent feedforward inhibition to the RS cells, the primary information encoders (Bruno, 2011; Petersen, 2007; Sun, Huguenard, and Prince, 2006; Cruikshank, Lewis, and Connors, 2007; Bruno and Simons, 2002; Keller and Carlson, 1999; Welker and Woolsey, 1974; Beaulieu, 1993; Kawaguchi and Kubota, 1993; Land, Buffer, and Yaskosky, 1995). The particular whisker driving a given barreloid/barrel module is termed the principal whisker (PW) of the module, and the feedforward (or phase-delayed) inhibitory structure within a barrel, a common motif in neuronal systems, ensures that RS cells within a barrel are most responsive to synchronous TC input originating from their PW (Patel and Joshi, 2013; Joshi and Patel, 2013; Bruno, 2011; Benowitz and Karten, 2004; Deng and Rogers, 1998; Sridharan, Boahen, and Knudsen, 2011; Patel and Reed, 2013; Mittmann, Koch, and Häusser, 2005; Fricker and Miles, 2000; Pouille and Scanziani, 2001; Wehr and Zador, 2003; Blitz and Regehr, 2005; Jortner, Farivar, and Laurent, 2007; Leitch, Laurent, et al., 1996; Perez-Orive et al., 2002; Liu, Patel, and Joshi, 2014).

Somatosensory receptors connected to a particular whisker on the mystacial pad encode bending moment (proportional to deflection angle) and the temporal derivative of bending moment (proportional to deflection velocity), and this information is relayed to the corresponding thalamic barreloid (Campagner et al., 2018). A barreloid employs a dual coding scheme, spike synchrony and spatial distribution of spiking responses, to simultaneously represent the velocity or angular direction, respectively, of a deflection of its PW. Larger PW deflection velocities leave net barreloid spike counts (and the spatial distribution of spike counts) unchanged while tightening the synchrony of population spiking (Pinto, Brumberg, and Simons, 2000; Bruno and Sakmann, 2006; Temereanca, Brown, and Simons, 2008)), while deflection direction is encoded via the spatial distribution of barreloid spikes – barreloid TC cells are anatomically segregated into direction groups, with cells within a fixed group responding most intensely to a preferred angular direction of PW whisker deflection (Timofeeva et al., 2003), and responses within the

group diminishing in spike output as PW deflection direction deviates away from the group's preferred direction and approaches the opposite direction 180° away (Bruno and Simons, 2002; Pinto, Brumberg, and Simons, 2000; Temereanca and Simons, 2003). Thus, individual barreloid TC cells exhibit direction tuning in terms of response magnitude, while velocity is not readily apparent from the response of an individual TC cell, but is encoded via barreloid-wide population synchrony.

Individual barrel RS cells, on the other hand, exhibit both velocity *and* direction tuning for the PW of the barrel. RS cells are segregated by PW direction preference into domains placed within an anatomical pinwheel structure (Bruno et al., 2003; Kremer et al., 2011; Andermann and Moore, 2006), and the response amplitude (i.e., spike output) of a barrel cell diminishes as the velocity of PW deflection decreases as well as if the direction of PW deflection deviates from the preferred direction of the barrel cell's direction domain (Bruno and Simons, 2002; Pinto, Brumberg, and Simons, 2000; Lee and Simons, 2004; Wilent and Contreras, 2005). Prior modeling work examines the role of bareloid input and feedforward inhibition in the dynamics of velocity and direction tuning for PW deflections in barrel RS cells (Patel, 2018b; Patel, 2018a).

However, empirical studies show that parallelization and segregation of information processing by whisker along the whisker→barreloid→barrel pathway is not an entirely accurate conceptual picture of the functional organization of the system. Indeed, at the level of the barrel, RS cells, while most strongly responsive to deflections of their corresponding PW, also respond, albeit more weakly and with higher latency, to adjacent whiskers (AWs) (Kwegyir-Afful et al., 2005; Simons and Carvell, 1989; Bruno and Simons, 2002; Armstrong-James, Fox, and Das-Gupta, 1992; Brecht and Sakmann, 2002a; Zhu and Connors, 1999). At the level of the barreloid, studies have shown that TC cells may also exhibit responses, though diminished in magnitude, to AWs (Timofeeva et al., 2004; Ghazanfar and Nicolelis, 1997; Lee, Friedberg, and Ebner, 1994; Brecht and Sakmann, 2002b; Bruno and Simons, 2002; Kwegyir-Afful et al., 2005; Simons and Carvell, 1989).

In this work, we are concerned with the AW responses of barrel RS cells, and in this regard, a natural query to pose is, 'at what level in the hierarchy of the barrel system does cross-talk between parallel whisker information streams occur?'. There are three possibilities for cross-whisker information transfer that gives rise to multiwhisker receptive fields within barrels: (i) RS cells simply inherit their AW responses from TC cells within the aligned barreloid that respond to multiple whiskers; (ii) RS cells, while predominantly receiving input from their aligned

barreloid, also receive input, albeit less substantially, from AW barreloids; (iii) RS cells receive AW input via lateral connections between cortical barrels (Katz, Heiss, and Lampl, 2006). A body of experimental literature exists that attempts to address this issue, though empirical results have often been contradictory and difficult to reconcile, and as of yet no consensus has been reached. The issue of which of the three possibilities, or combination of the three, is responsible for the origin of multiwhisker RC cell receptive fields therefore remains an open question.

Several lines of evidence provide support for possibility (i). Multiple studies have directly measured AW responses of TC cells (Timofeeva et al., 2004; Ghazanfar and Nicolelis, 1997; Lee, Friedberg, and Ebner, 1994; Brecht and Sakmann, 2002b; Bruno and Simons, 2002; Kwegyir-Afful et al., 2005; Simons and Carvell, 1989), though such studies do not establish that the AW responses of TC cells are actually responsible for multiwhisker RS cell receptive fields. Indirect evidence suggesting that multiwhisker TC cell receptive fields causally generate multiwhisker RS cell receptive fields is provided by one study that showed induction of a brainstem lesion to reduce AW responses of TC cells substantially reduces AW responses of RS cells as well (Kwegyir-Afful et al., 2005), along with another study in which spike cross-correlograms of TC cell pairs are shown to be suggestive that PW and AW responses of RS cells arise from the same TC cells (Bruno and Simons, 2002). Furthermore, a couple of studies provide general support for a feedforward mechanism of multiwhisker RS cell receptive field generation (i.e., possibilities (i) and (ii)). Results from one study show that responses to a fixed whisker in neighboring barrels persist following ablation of the fixed whisker's barrel, suggesting that lateral barrel-to-barrel connections are not responsible for AW responses (Goldreich, Kyriazi, and Simons, 1999); another study shows that barrel cells continue to display subthreshold AW responses following suppression of spiking in all barrels via broad application of a GABA agonist throughout barrel cortex, again suggesting that lateral connections are not needed for AW input to reach barrel cells (Roy, Bessaih, and Contreras, 2011).

Direct support for possibility (ii) is rather sparse. One study suggests a possible anatomical substrate for possibility (ii) by showing that some TC axons branch into adjacent (nonaligned) barrels, with such axons exhibiting considerable (66%) arborization within AW barrels (Arnold, Li, and Waters, 2001); however, several other investigations have failed to find significant connections from TC cells to any AW barrels (Agmon et al., 1995; Bruno and Simons, 2002; Land, Buffer, and Yaskosky, 1995; Bernardo and Woolsey, 1987; Jensen and Killackey, 1987; Bruno and Sakmann, 2006). Thus, of the two feedforward mechanisms of multiwhisker RS cell receptive

field generation, possibility (*i*) appears to be the most compelling.

However, there also exist multiple studies providing evidence for the lateral interaction hypothesis of RS cell AW responses (possibility (*iii*)). In contrast to the studies mentioned above (Goldreich, Kyriazi, and Simons, 1999; Roy, Bessaih, and Contreras, 2011), other studies indicate that lateral connections between barrels are indeed necessary for multiwhisker RS cell receptive fields to emerge. In one study, abolishing spiking within a fixed barrel (via GABA agonist application) prevented responses to that barrel's PW in neighboring barrels, and reactivation of a single barrel with a GABA antagonist (while the remainder of barrel cortex remained suppressed by a GABA agonist) abolished all AW responses in the reactivated barrel (Fox et al., 2003). Another study shows that responses to a fixed whisker in neighboring barrels are reduced in direct proportion to the extent of lesioning of the fixed whisker's barrel (Fox, 1994). Moreover, several studies provide more indirect support for possibility (*iii*). For example, focal caged glutamate photolysis reveals that substantial inputs to RS cells from neighboring barrels exist (Schubert et al., 2003), along with several investigations indicating either anatomical or functional connectivity among neighboring barrels (Brecht and Sakmann, 2002a; Petersen and Sakmann, 2001). It should be noted that lateral barrel-to-barrel connections may not involve direct layer IV to layer IV synapses, as arborization of layer IV cells may be largely confined to the barrel of origin (Harris and Woolsey, 1983; Lubke et al., 2000; Petersen and Sakmann, 2000); rather, nongranular layers may provide the medium for interbarrel information transfer (Gottlieb and Keller, 1997), with AW information relayed to layer IV via intrabarrel connections from nongranular layers (Thomson et al., 2002).

Evaluating the competing possibilities – namely, feedforward versus lateral – for multiwhisker RS cell receptive field generation within the context of existing experimental data may provide important insights into the mechanisms at play. In prior modeling work (Patel, 2019), we study in detail the ability of possibility (*i*) to account for the available physiological data. In this study, we employ a modeling approach to examine the viability of possibility (*iii*) in explaining empirical observations.

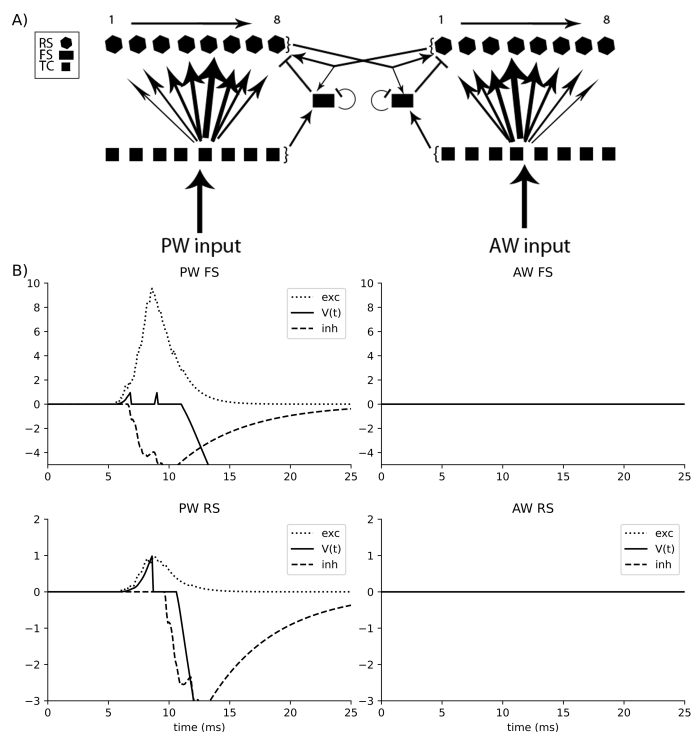


Figure 1. Model schematic of two-barreloid/barrel system corresponding to nearby whiskers on the mystacial pad, with one designated the PW and the other the AW (A) and FS and RS cell responses to whisker deflections in the absence of lateral connections (B). A) Schematic of model with lateral connections between barrels. Arrow heads indicate excitation; bar heads indicate inhibition. Within each barreloid, 240 TC cells are divided into 8 direction groups, with each group assigned a preferred deflection direction for its corresponding whisker. 160 RS cells within each barrel are split into 8 direction domains for deflections of their corresponding whisker, with each domain aligned to the TC direction group shown directly below. RS direction domains and TC direction groups labeled numerically at the top of the schematic (1=180°, 2=225°, 3=270°, 4=315°, 5=0°, 6=45°, 7=90°, 8=135°). The density of TC→RS synapses depends on TC group-RS domain alignment; the diagram shows connection densities from a sample TC group (line/arrow thickness represents synapse density). Within a barreloid/barrel system, TC cells uniformly excite a population of 100 FS cells, which uniformly inhibit themselves as well as the RS cell population. Reciprocal connections between barrels are in the form of randomly wired RS→RS and RS→FS synapses. Deflections of the whisker designated PW or AW are simulated by excitation of TC cells within the PW or AW barreloids, respectively, with TC cells responding only to deflections of their corresponding whisker. TC cells are not explicitly simulated; rather, spike times of TC cells are randomly determined at the beginning of a trial. Deflection direction determines the probability of a TC cell spike in accordance with its direction preference. See *Methods* for details. B) Plots of membrane potential, net excitation, and net inhibition over time to a single FS (top row) or RS (bottom row) cell within the PW barrel during a single trial, for either a PW (right column) or AW (left column) deflection, in the absence of lateral connections between barrels. Excitatory currents result solely from feedforward TC input and inhibitory currents arise solely from intra-barrel FS cells. Deflection direction is set at the preferred PW or AW deflection angle of the cell for PW or AW deflections, respectively.

2.2 Results

Figure 1A shows a schematic of the model of two barreloid/barrel systems, corresponding to two nearby whiskers on the mystacial pad, with lateral connections between barrels. Each barreloid/barrel system incorporates 240 TC cells divided into 8 PW direction groups of 30 cells each (Land, Buffer, and Yaskosky, 1995), with each direction group assigned a preferred direction of PW deflection (Timofeeva et al., 2003); in order to isolate the effects of lateral barrel-to-barrel connections, TC cells in the model do not respond to AW deflections. TC cells are not explicitly modeled; each cell spikes either 0 or 1 times per PW deflection, and the times of TC spikes are drawn from a distribution similar to the experimentally observed TC spike time distribution (Pinto, Brumberg, and Simons, 2000). To simulate a PW whisker deflection of a particular angular direction, TC cells within the corresponding PW direction group spike with high probability, while spike probability progressively diminishes in TC direction groups whose preferred PW directions deviate from the stimulus direction, with the lowest spike probability in the TC group with a preferred direction 180° away.

Within a barreloid/barrel system, the 240 TC cells drive a small population of 100 FS cells (Lee and Simons, 2004; Simons and Carvell, 1989; Bruno and Simons, 2002; Swadlow and Gusev, 2002), and the FS cells inhibit a pool of 160 RS cells. The RS cells are organized into 8 PW direction domains (Kremer et al., 2011; Andermann and Moore, 2006), with each RS domain aligned with a TC direction group (and assigned the corresponding direction label). The density of TC→RS synapses depends upon TC group-RS domain alignment – the probability that a TC cell synapses onto an RS cell diminishes as the PW direction domain of the RS cell deviates from the PW direction group of the TC cell, with the probability assuming a minimal value if the direction label of the RS domain differs by 180° from the direction preference of the TC cell (Bruno and Simons, 2002; Bruno et al., 2003; Furuta, Deschenes, and Kaneko, 2011); the diagram in figure 1 shows connection densities from the TC group with a preferred PW direction of 0° to RS PW direction domains (with analogous connectivity for other TC direction groups). Thus, biased intrabarrel TC→RS synaptic connectivity (based on direction preference) imbues barrel RS cells with directional tuning for PW deflections. Reciprocal lateral connections between barrels are random and independent of direction preference, and consist of RS→RS and RS→FS synapses. Model details and experimental justification of parameter values can be found in the *Methods* section.

Figure 1B shows the response of an FS or RS cell within the PW barrel to a PW or AW deflection, in the case that lateral connections between barrels are removed from the model. In this scenario, responses to PW deflection remain largely unaffected relative to the model with intact lateral connections (compare with figure 2A), while responses to AW deflection do not occur. Responses to PW deflection are unaffected because PW deflections only trigger TC cells within the PW barreloid, and the feedforward mechanism by which this excitation is transferred to the PW barrel remains intact. The latter observation is a direct consequence of the lack of lateral connections – within the model, AW deflections trigger only TC cells within the AW barreloid, and without lateral connections the model contains no mechanism for this excitation to reach the PW barrel.

2.2.1 Single Whisker Deflections

Figure 2A compares single cell responses to PW and AW deflections in terms of membrane potential and net incoming excitatory or inhibitory current over time. For a single RS or FS cell, excitation is summed over local TC input and lateral RS input, while inhibition arises from only local FS input. Experimentally, responses to AW deflection, relative to responses to PW deflection, are characterized by lower spike counts – responses for FS and RS cells report average spike responses of between 40-80% and 20-60% respectively, relative to PW responses, with RS cell activity typically skewing toward the lower end of that range (Schubert et al., 2003; Fox et al., 2003; Kyriazi and Simons, 1993; Bruno and Simons, 2002; Armstrong-James, Fox, and Das-Gupta, 1992) – and longer latencies (Brecht and Sakmann, 2002a). Within the model, both RS and FS cells indeed show stronger central receptive fields for their PW and weaker surround receptive fields for the AW, with FS cells having a slightly stronger response to AW deflections than RS cells (Kwegyir-Afful et al., 2005; Simons and Carvell, 1989; Bruno and Simons, 2002; Armstrong-James, Fox, and Das-Gupta, 1992; Brecht and Sakmann, 2002a; Zhu and Connors, 1999). This occurs because lateral connections are relatively weak in comparison to feedforward connections and excitatory currents generated by AW deflections must first traverse through their home (AW) barrel before reaching their target FS and RS cells in the PW barrel. In particular, excitation delivered by the AW barrel is effectively subjected to two waves of inhibition – AW RS cells receive inhibition from AW FS cells, reducing their net response, while lateral connections from AW RS cells to the PW barrel trigger both PW FS and RS cells, entailing inhibition

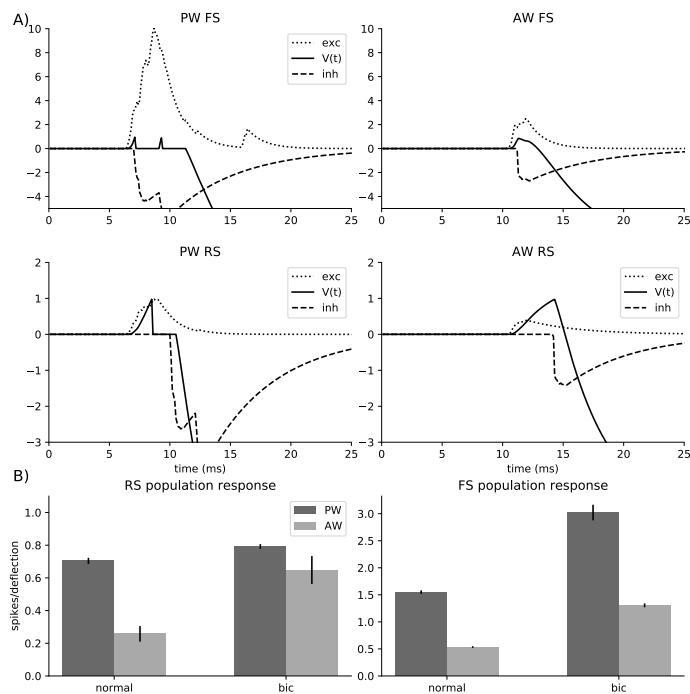


Figure 2. Single cell (A) and population responses (B) of FS and RS cells in the PW barrel to PW and AW deflections. A) Plots of membrane potential, net excitation, and net inhibition over time to a single cell during a single trial. Excitatory currents result from a combination of feedforward TC input and lateral input from the AW barrel for responses to PW deflections (left), and solely from lateral connections for responses to AW deflections (right). Inhibitory currents arise solely from intra-barrel FS cells. Top panels show FS cells and bottom panels show RS cells. Deflection direction is set at the preferred PW or AW deflection angle of the cell for PW or AW deflections, respectively. B) Spikes per deflection averaged over all RS (right panel) and FS (left panel) cells within the PW barrel before and after bicuculline application, for both PW and AW deflections. Standard deviations are taken over 100 trials. Bicuculline application is simulated by suppressing all GABA synapses by 95%. PW and AW deflections are at an angular direction of 0° .

of PW RS cells by PW FS cells. Longer latencies within the model to AW deflection arise as a consequence of synaptic delay – excitation from PW deflection traverses a single synapse to reach PW barrel RS cells, while excitation from AW deflection must traverse two synapses to reach PW barrel RS cells (latencies are further quantified in in figure 7).

Figure 2B shows FS and RS population firing rates in the normal network as well as under simulated application of the GABA antagonist bicuculline, in which the strength of GABA synapses is reduced by 95%. Blockage of model GABA synapses in the context of PW deflections shows a notable but relatively small increase in the activity of barrel RS cells, while in the context of AW deflections RS cells display a markedly greater increase in activity, indicating that (in the intact network) inhibition exhibits a disproportionately large suppressive effect on weaker AW

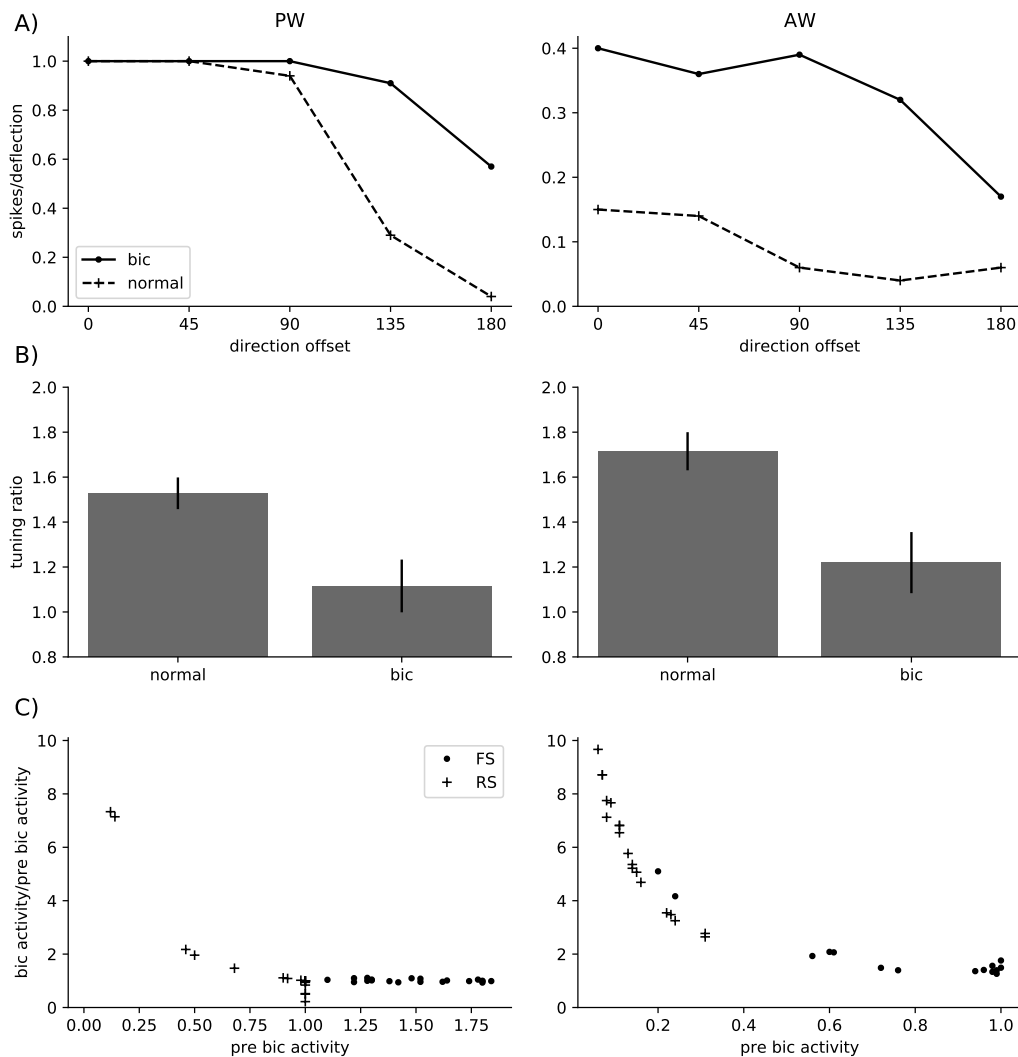


Figure 3. RS cell response to application of bicuculline, simulated by suppressing all GABA synapses by 95%. A) Tuning curves of a single RS cell in response to PW (left) or AW (right) deflection. Tuning curves are plotted as average spikes per deflection vs direction offset (the angular distance of deflection direction from the preferred direction of the cell). Responses are averaged over angular directions equidistant from the preferred direction of the cell and calculated over 100 trials. B) Average tuning ratio across all RS cells within the PW barrel, calculated as response to preferred direction/average response over all directions. Error bars represent population standard deviations. C) Scatter plot of single cell responses; the ratio of post-bicuculline to pre-bicuculline response is shown on the y-axis and pre-bicuculline activity is shown on the x-axis, for PW (left) and AW (right) deflection. Data are shown for 20 RS and FS cells. Responses are averaged over 100 trials. For both PW or AW deflections, deflection direction is set at the preferred PW or AW deflection angle, respectively, of each cell.

responses than on stronger PW responses, in accordance with experiment (Kyriazi et al., 1996; Fox et al., 2003). Within our model, excitation to RS cells within the PW barrel following an AW deflection would normally be subjected to two waves of inhibition (first in the AW barrel, then in

the PW barrel, as described above); hence, in the absence of significant inhibition, the normally weak AW response is disproportionately increased relative to the PW response, and disinhibited AW responses are only slightly weaker than disinhibited PW responses. Experiments further show that, in general, barrel cells that exhibit lower levels of activity in response to a fixed stimulus prior to bicuculline application tend to display higher amplifications in spiking response following bicuculline application (Kyriazi et al., 1996), a result captured by our model in figure 3C. The role of inhibition in preferentially and disproportionately suppressing weaker responses also comes into play in the dynamics of paired whisker deflections (details in the *Paired Whisker Deflections* section below).

Direction tuning properties of RS cells within our model are summarized in figure 3A and 3B, showing that RS cells within the model exhibit direction tuning in response to both PW deflections (Bruno and Simons, 2002; Pinto, Brumberg, and Simons, 2000; Lee and Simons, 2004; Wilent and Contreras, 2005; Bruno et al., 2003; Kremer et al., 2011; Andermann and Moore, 2006) and AW deflections (Hemelt et al., 2010; Simons and Carvell, 1989; Kyriazi et al., 1996; Kida, Shimegi, and Sato, 2005). PW direction tuning in the model arises due to the structure of feedforward connectivity, since TC \rightarrow RS cell synaptic density within the PW barrel is dependent upon the PW direction preferences of TC cells (Patel, 2018b; Patel, 2018a); see Methods for details. Lateral connections between barrels, however, are random and independent of direction preference; AW direction selectivity arises due to a somewhat similar mechanic to that observed in previous work (Patel, 2019) – such selectivity results from an RS cell within the PW barrel receiving, by chance, a plurality of its lateral input from RS cells within the AW barrel with a common AW direction preference. The dominant AW direction preference in the lateral input to a PW RS cell instills a direction preference in the cell, yielding a stronger response to the overrepresented AW direction and diminishing responses for deviations away from this preferred AW direction. We note that these dual mechanisms of generating PW and AW direction tuning imply that, within our model, the AW direction preference of an RS cell is determined essentially randomly and hence is unrelated to its PW direction preference as determined by structured feedforward input (figure 4C), a feature also observed experimentally (Hemelt et al., 2010; Simons and Carvell, 1989; Le Cam et al., 2011). Figure 3B also shows that, in accordance with experiment (Kyriazi et al., 1996), bicuculline application within the model results in weaker PW and AW direction tuning, which occurs as a consequence of disinhibition preferentially amplifying weaker responses (i.e., responses to PW or AW deflection directions far from the preferred directions of the cell) more

so than stronger responses (i.e., responses to deflection directions near the preferred directions of the cell). As observed empirically (Lee and Simons, 2004; Simons and Carvell, 1989; Bruno and Simons, 2002), FS cells within the model exhibit little direction selectivity (data shown in supplementary figure S1) – the lack of direction preference in the feedforward input to FS cells ensures a lack of PW direction selectivity, and the strength of lateral synapses to FS cells entails a lack of AW direction selectivity.

2.2.2 Paired Whisker Deflections

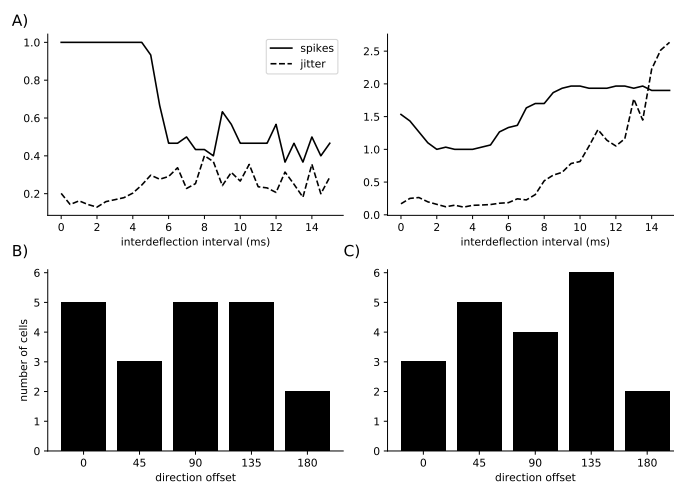


Figure 4. Responses of single and groups of RS cells to paired whisker deflections. A) Spikes per deflection and jitter of a single RS cell in response to a PW deflection preceded by AW deflection, plotted as a function of interdeflection interval. Jitter is calculated as the standard deviation of the timing in the first spike following PW deflection. Spike response is examined with (right) and without (left) bicuculline application, which is simulated by reducing the strength of GABA synapses by 95%. AW and PW deflection directions are at the preferred AW and PW angular directions of the cell, respectively. Data gathered over 50 trials. B) Distribution over 20 RS cells of the AW deflection angle that yields maximum suppression of the PW response in a paired whisker deflection; the x-axis shows direction offset for the AW deflection (AW deflection angle as distance in degrees from preferred PW deflection direction), while bars show the number of RS cells for which each AW direction offset maximized suppression of the subsequent PW response. Interdeflection interval is set at 8.5 ms. C) For single whisker deflections, distribution over 20 RS cells of preferred AW deflection angles, with direction offset for AW deflections (AW deflection angle as distance in degrees from preferred PW deflection direction) plotted on the x-axis.

Experiments show that in a paired deflection protocol – an AW deflection preceding a PW deflection – the prior AW deflection tends to have a suppressive effect on the response of the RS cell to the subsequent PW deflection (Brumberg, Pinto, and Simons, 1996; Kyriazi et al., 1996;

Goldreich, Kyriazi, and Simons, 1999; Higley and Contreras, 2007). As the interdeflection interval (IDI) approaches 10 ms, suppression approaches its maximum, with the suppressive effect gradually vanishing as IDI is increased up to 100 ms (Shimegi et al., 1999; Simons, 1985; Simons and Carvell, 1989). Our model exhibits similar behavior. Figure 4A shows spike counts and jitter plotted as a function of IDI, both in the intact network (figure 4A-left) and after simulation of bicuculline application (figure 4A-right). With inhibition present (figure 4A-left), suppression begins at an IDI of ~ 4 ms and plateaus as IDI approaches 10 ms. This occurs within the model as a consequence of lateral input from the AW barrel triggering FS cell activity within the PW barrel; the latency of lateral input from the AW barrel, in combination with the synaptic delay generated by the time course of FS cell activation and inhibitory transmission within the PW barrel, entails a delay in inhibition to PW barrel RS cells. The lingering, delayed inhibition triggered by the AW deflection then serves to suppress responses to the subsequent PW deflection, provided the IDI is sufficiently large to ensure that the PW deflection does not occur prior to the arrival of inhibition triggered by the AW deflection. Additionally, as observed experimentally (Simons, 1985), within our model jitter in the timing of the first spike following PW deflection tends to increase as suppression increases with IDI. Blockade of GABA synapses within the model (figure 4A-right) abolishes the suppressive effect of prior AW deflection on subsequent PW deflection, indicating the effect is mediated by synaptic inhibition, in accordance with experiment (Kyriazi et al., 1996); jitter in spike timing also increases dramatically in the bicuculline condition, due to a lack of feedforward inhibition triggered by the PW deflection that would normally serve to sharply curtail the temporal window within which an RS cell is constrained to fire.

Empirical investigations further examine the effect of angular direction of AW deflection on suppression of a subsequent PW deflection in a paired deflection protocol, showing that the AW deflection angle that generates maximal suppression is independent of and often quite different from an RS cell's preferred PW deflection direction (Simons and Carvell, 1989; Simons, 1985). Our model also captures this behavior. Figure 4B shows that among 20 RS cells within the model with a common PW direction preference, the AW deflection angle that causes maximal suppression in a paired deflection protocol varies from cell to cell and bears little relation to PW direction preference.

Figure 5A examines the effects of prior AW deflection on the directional tuning properties of PW barrel RS cells to subsequent PW deflections. In accordance with experiment (Brumberg,

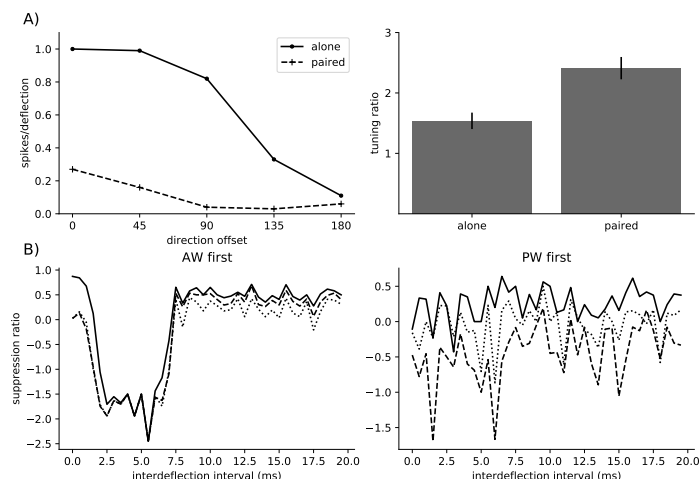


Figure 5. Effect of prior AW deflection on PW direction tuning and effects of changing the temporal order of deflections in paired deflection protocols. A) Left: PW tuning curve of a sample RS cell in the case of isolated PW deflection versus PW deflection preceded by AW deflection. Direction offset represents angular distance of PW deflection direction from preferred PW direction; responses are averaged over directions equidistant from preferred. Interdeflection interval is set at 8.5 ms; AW deflections are at the preferred AW deflection angle of the cell. Data gathered over 100 trials. Right: PW tuning ratio (response to preferred direction/average response over all directions) for PW deflections preceded by AW deflection, averaged across a population of cells within the same PW direction group of 0° . AW deflection direction is fixed at 0° ; interdeflection interval is set to 8.5 ms. B) Left: Suppression ratio for paired deflections, where AW deflection precedes PW deflection, for 3 sample RS cells as a function of interdeflection interval. Positive values indicate suppression, and negative values indicate facilitation. Suppression ratio is calculated as ((response to PW alone - response to PW deflection following AW deflection)/response to PW alone). For the prior AW deflection, direction is set at 0° . Right: Suppression ratio for paired deflections, where PW deflection precedes AW deflection, for the same 3 sample RS cells as in left panel, as a function of interdeflection interval. Positive values indicate suppression, and negative values indicate facilitation. Suppression ratio is calculated as ((response to AW alone - response to AW deflection following PW deflection)/response to AW alone). For the prior PW deflection, direction is set at 0° .

Pinto, and Simons, 1996), prior AW deflection does not qualitatively affect the PW direction preference of a model RS cell (figure 5A-left) but sharpens directional tuning and hence increases tuning ratio for the PW (figure 5A-right), in comparison to isolated PW deflections. This occurs as a consequence of the disproportionately large impact of inhibition on weaker responses (Kyriazi et al., 1996; Fox et al., 2003); the inhibition generated by prior AW deflection has a larger suppressive effect on weaker responses to subsequent PW deflection than stronger ones – namely, responses to PW deflection directions farther from preferred are suppressed to a greater extent than responses to those closer to preferred.

Empirical investigations show that, while paired deflections in general tend to result in a suppressive effect of the prior deflection on the subsequent deflection in an RS cell, in some cases facilitation is observed. Paired deflections in which AW deflection precedes PW deflection tend to be consistently suppressive, with only $\sim 20\%$ of RS cells not showing notable suppression of the subsequent deflection (for sufficiently large IDIs) (Simons and Carvell, 1989); in contrast, when the order of deflections is reversed (i.e., PW deflection preceding AW deflection) a wider range of possible responses is observed and pronounced facilitation tends to be more common (Simons, 1985). In order to assess this phenomenon within our model, we employ a metric termed the suppression ratio, with values above zero indicating a suppressive effect and values below zero indicating a facilitatory effect of the prior deflection on the response to the subsequent deflection. Figure 5B plots the suppression ratio for several typical model RS cells, showing both suppression and facilitation in an IDI dependent manner. In the case of AW preceding PW deflection (figure 5B-left), facilitation tends to occur for small IDIs, due to the latency in the response to AW deflection (relative to PW deflection) causing excitation from the two deflections to overlap for small IDIs prior to the arrival of inhibition triggered by either deflection; for larger IDIs, on the other hand, suppression tends to occur, as inhibition triggered by prior AW deflection suppresses the response to subsequent PW deflection. In the case of PW preceding AW deflection (figure 5B-right), however, suppression ratio curves as a function of IDI tend to be more irregular, due to the complex interplay between strong, lingering excitation from prior PW deflection, synaptically delayed weak excitation from subsequent AW deflection, and inhibition triggered by the prior PW deflection.

It is important to note that while there is empirical evidence that lateral barrel-to-barrel connections exist (Schubert et al., 2003; Brecht and Sakmann, 2002a; Petersen and Sakmann, 2001), such lateral connections are as of yet poorly characterized in the experimental literature, and it is possible that they do not involve direct layer IV to layer IV connections, but rather multi-synaptic connections traversing through intermediary nongranular layers (Harris and Woolsey, 1983; Lubke et al., 2000; Petersen and Sakmann, 2000; Gottlieb and Keller, 1997; Thomson et al., 2002). Thus, our model of lateral connectivity is by necessity a simplification, intended only to provide a general framework within which to assess the effects of interbarrel communication. The lack of detailed anatomical data on interbarrel connections, however, implies that, unlike for the parameters governing intrabarrel architecture and synaptic dynamics, the connectivity and synaptic strength parameters for interbarrel communication within our model are necessarily

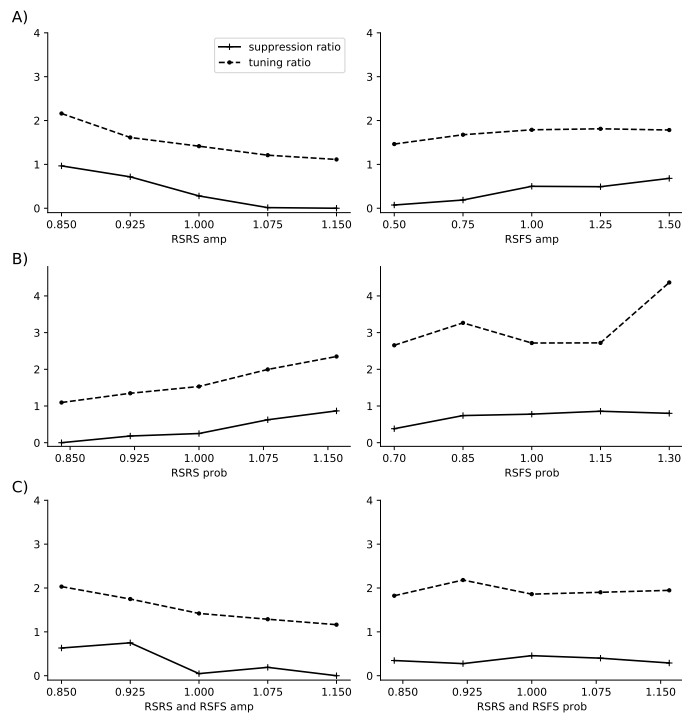


Figure 6. Effects of varying the probability and/or strength of lateral connections between the PW and AW barrel on suppression ratios and AW tuning ratios of RS cells within the PW barrel. Tuning ratio is calculated for single AW whisker deflections as response to preferred direction/average response over all directions; suppression ratio is calculated for paired deflections as ((response to PW alone - response to PW after prior AW deflection)/response to PW alone). Data are averaged over all RS cells in the PW barrel. For paired whisker deflections, AW deflection angle is set at 0° , PW deflection angle is set at the preferred PW direction of the cell, and interdeflection interval is set to 8.5 ms. A) Tuning and suppression ratio of RS cells within the PW barrel as a function of the strength of RS→RS (left) or RS→FS (right) synapses from the AW barrel to PW barrel. On the x-axis, strengths shown are relative to standard model values (1 represents the standard strength employed in the model). B) Tuning ratio and suppression ratio of RS cells within the PW barrel as a function of the connection probability of RS→RS (left) or RS→FS (right) synapses from the AW barrel to the PW barrel. On the x-axis, connection probabilities shown are relative to standard model values (1 represents standard connection probability). In order to isolate the effect of connection probability, changes in connection probability are accompanied by a proportional but inverse change in synaptic strength. C) Tuning ratio and suppression ratio of RS cells within the PW barrel as a function of simultaneous variation of RS→RS (left) and RS→FS (right) synapses from the AW barrel to the PW barrel, for synaptic strength (left) and connection probability (right). On the x-axis, values shown are relative to standard model values (1 represents standard value).

somewhat arbitrary. It is therefore important to assess the effects on model dynamics of varying these latter sets of parameters and to ensure that reasonable dynamics emerge from a range of physiologically realistic parameter values.

Accordingly, figure 6 shows that RS cells within the PW barrel exhibit reasonable suppression ratios for paired deflections and AW tuning ratios for single AW deflections over a range of parameter values, as RS→RS and RS→FS interbarrel synapses are varied separately or simultaneously. Figure 6A (left) shows that increasing the strength of interbarrel RS→RS synapses (while keeping interbarrel connectivity fixed) tends to decrease both AW tuning ratio and suppression ratio. The former observation is due to stronger RS→RS interbarrel excitation (with fixed architecture) dampening the disparate effect of inhibition on stronger versus weaker responses (since responses to AW deflections far from the preferred direction are now stronger, the tendency of inhibition to suppress these responses more than responses to deflections closer to the preferred direction is reduced); the latter observation is due to stronger RS→RS interbarrel excitation yielding higher amplitude responses to prior AW deflection, with excitation due to prior AW deflection lingering for a longer period of time and hence more efficaciously augmenting the response to subsequent PW deflection. Figure 6A (right), on the other hand shows that increasing the strength of RS→FS interbarrel excitation (while keeping interbarrel connectivity fixed) tends to increase AW tuning ratio and suppression ratio; this is due to increased inhibition within the PW barrel from AW deflection – increased inhibition tends to preferentially suppress weaker responses to isolated AW deflections (increasing the AW tuning ratio) as well as having a greater suppressive effect on a subsequent PW deflection (increasing the suppression ratio). Increasing the density of interbarrel synapses (while keeping synaptic amplitudes fixed) tends to have similar, though less pronounced, effects (data shown in supplementary figure S2).

Figure 6B examines the effects of increasing interbarrel RS→RS (figure 6B-left) or RS→FS (figure 6B-right) synaptic density, while commensurately diminishing RS→RS or RS→FS synaptic strength, respectively; thus, RS→RS or RS→FS synaptic density is varied while fixing the average level of excitation received by RS or FS cells, respectively, within the PW barrel. Figure 6B (left) indicates that increasing interbarrel RS→RS synaptic density tends to increase the AW tuning ratio as well as the suppression ratio for PW barrel RS cells, suggesting that the commensurate decrease in synaptic strength has a more pronounced effect than the increase in synaptic density (this is likely due to standard RS→RS interbarrel connectivity being rather high at a 0.7 connection probability, with small changes hence yielding a smaller-magnitude effect in comparison to similar fractional changes in synaptic strength in the reverse direction). Figure 6B (right) shows that increasing interbarrel RS→FS synaptic density produces little systematic impact on the AW tuning ratio or suppression ratio of PW barrel RS cells, likely due to the significantly

lower standard value of 0.4 for RS→FS interbarrel connectivity (hence small changes yield a similar-magnitude effect in comparison to similar fractional changes in synaptic strength in the reverse direction, with the two changes effectively canceling each other).

We also study the effects of varying interbarrel RS→RS and RS→FS synapses simultaneously (and in the same direction), with synaptic strength varied in figure 6C (left) and synaptic density varied in figure 6C (right). Figure 6C (left) shows that simultaneously increasing cross-barrel RS→RS and RS→FS synaptic strengths tends to decrease the AW tuning ratio and suppression ratio of PW barrel RS cells; the similarity to figure 6A (left) suggests that the system is somewhat more sensitive to changes in the amplitude of excitatory synapses than inhibitory synapses, likely due to the higher density of cross-barrel excitatory synapses relative to inhibitory synapses. Figure 6C (right), on the other hand, shows that simultaneously increasing cross-barrel RS→RS and RS→FS synaptic density has little effect on the AW tuning ratio and suppression ratio of PW barrel RS cells, indicating the maintenance of a relative balance of the opposite effects of increasing excitation versus inhibition in the system.

2.2.3 Three Barrel Model

Experiments employing multiple AWs suggest that the response of an RS cell to AW deflection depends on the physical distance on the mystacial pad of the deflected AW to the PW of the cell (where distance is measured in terms of the number of intervening whiskers between the AW and PW); namely, as distance on the mystacial pad increases, the peak excitation induced in the RS cell by AW deflection diminishes in magnitude (Kwegyir-Afful et al., 2005; Simons and Carvell, 1989; Bruno and Simons, 2002; Armstrong-James, Fox, and Das-Gupta, 1992; Brecht and Sakmann, 2002a; Zhu and Connors, 1999) while its spiking response increases in latency, with a latency increase of ~ 2 ms per unit distance (one whisker) (Armstrong-James, Fox, and Das-Gupta, 1992; Brecht and Sakmann, 2002a; Zhu and Connors, 1999; Le Cam et al., 2011). While the physiological mechanisms underlying these observations have yet to be fully elucidated, it is possible that these results are a consequence of barrel-to-barrel connectivity being dependent on mystacial pad separation – i.e., the possibility that barrels corresponding to nearby whiskers are more strongly interconnected than barrels corresponding to more distant whiskers. In order to examine this hypothesis, we add a third barreloid/barrel system to our model, labeling one barrel system as the PW, another as AW1 (to represent an AW one whisker away from the PW on the mystacial pad), and the third as AW2 (to represent an AW two whiskers away from the

PW but one whisker away from AW1 on the mystacial pad). Intrabarrel and interbarrel connectivity and synaptic strengths are kept identical to the two barrel model, except barrel-to-barrel connections exist only between barrels corresponding to immediately adjacent whiskers (i.e., $PW \leftrightarrow AW1$, $AW1 \leftrightarrow AW2$ connections but no $PW \leftrightarrow AW2$ connections).

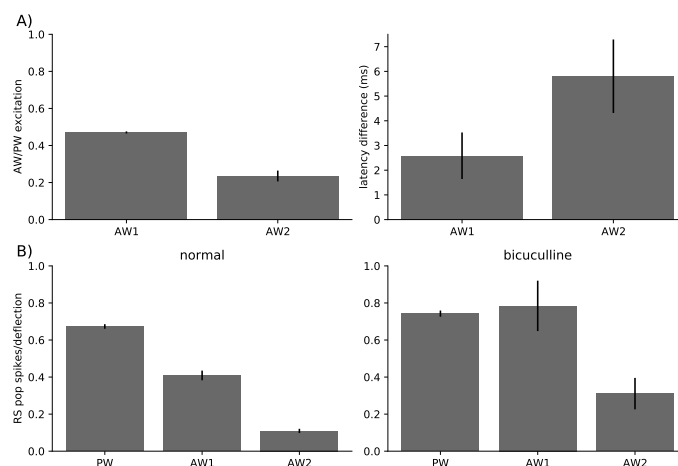


Figure 7. Dynamics of the three barrel model, with a barrel for the principal whisker (PW), a barrel for an immediately adjacent whisker (AW1), and a barrel for a third whisker (AW2) that is immediately adjacent to AW1 but more distant from the PW. Lateral connections between barrels exist only for immediately adjacent whiskers (i.e., $PW \leftrightarrow AW1$, $AW1 \leftrightarrow AW2$). A) Left: Ratio of peak excitation induced in a PW barrel RS cell by AW1 or AW2 deflection to peak excitation induced by the incoming excitatory current over the temporal duration of a deflection trial. Peak excitation is defined as the maximum value attained by the incoming excitatory current over the temporal duration of a deflection trial. Right: Latency to first spike for AW1 or AW2 deflection minus latency to first spike for PW deflection. B) Spikes/deflection of a PW barrel RS cell in the normal network (left) and after simulation of bicuculline application (right), in response to PW, AW1, or AW2 deflection. Bicuculline application is simulated by reducing the strength of GABA synapses by 95%. For all panels, single RS cell data are averaged over 100 trials and an error bar shows standard deviation in the mean of all RS cells in the PW barrel; PW and AW deflection angles are set at 0° for all trials.

Figure 7A shows that our model captures the empirical observations mentioned above – relative to PW deflection, the peak excitation induced in a PW RS cell diminishes (figure 7A-left) and spiking latency increases (figure 7A-right) more for AW2 deflection than for AW1 deflection. This occurs because AW2 deflections must first activate RS cells in the AW2 barrel, which in turn excites the AW1 barrel, and only then can excitation be transmitted to the PW barrel (while AW1 deflection immediately activates the AW1 barrel, which directly transmits excitation to the PW barrel). Thus, AW2 deflection leads to diminished excitation of the AW1 barrel relative to the AW2 barrel, and further diminished excitation of the PW barrel, leading to lower peak excitation

in the PW barrel in comparison to AW1 deflection, and the requirement for transmission of excitation through intervening synapses within the AW1 barrel entails longer spike latencies in the PW barrel relative to AW1 deflection. We note that these results follow naturally from a model in which multiwhisker receptive fields are due to lateral barrel connections (and where interbarrel connectivity is dependent on whisker distance on the mystacial pad), but are difficult to capture in our previous model in which multiwhisker receptive fields are generated by feedforward TC input (Patel, 2019).

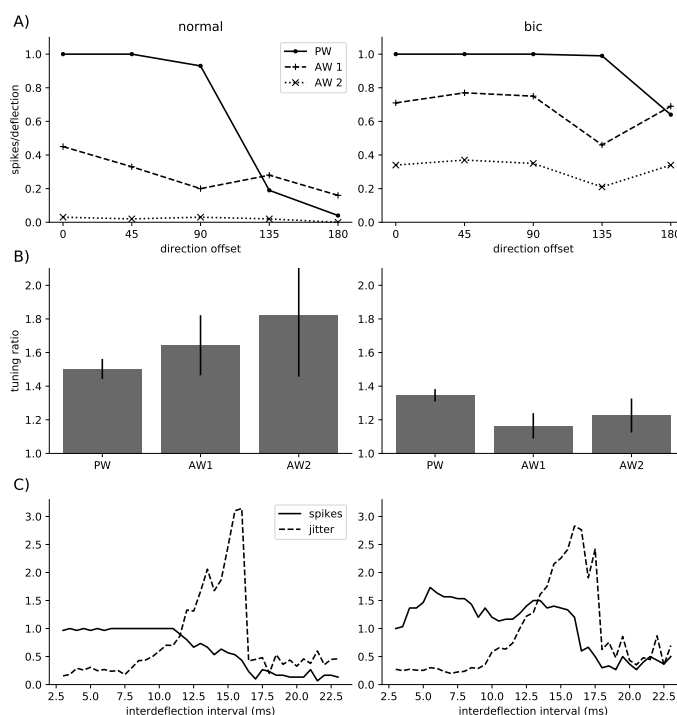


Figure 8. Dynamics of the three barrel model in the intact network (left columns of A,B,C) and following simulation of bicuculline application (right columns of A,B,C). A) PW, AW1, and AW2 tuning curves for a sample RS cell in the PW barrel. Tuning curves are plotted as average spikes per deflection versus direction offset (the angular distance between deflection direction and the preferred PW, AW1, or AW2 direction of the cell). Data are averaged over directions equidistant from preferred. Data are gathered over 100 trials. B) PW, AW1, and AW2 tuning ratios for a PW barrel RS cell, calculated as spikes per deflection for preferred direction/average spikes per deflection over all directions, averaged across all RS cells in the PW barrel. Error bars represent population standard deviations. Data are gathered over 100 trials. C) Response to PW deflection when preceded by AW2 deflection in a paired deflection protocol, as a function of interdeflection interval. Spikes per deflection (following PW deflection) and jitter (standard deviation in the timing of the first spike following PW deflection) are shown for a sample RS cell within the PW barrel. Data gathered over 50 trials.

Figures 7B and 8 examine the effects of simulating bicuculline application on the dynamics

of the three barrel model, with figure 7B showing, as expected, that spiking responses of PW RS cells increase after bicuculline simulation, and that weaker responses (those to AW1 and AW2 deflection) are preferentially enhanced by disinhibition in comparison to stronger responses (those to PW deflection). Sample PW RS cell tuning curves (figure 8A) and PW RS cell tuning ratios (figure 8B) show that in the intact network, relative to PW direction tuning, tuning ratios tend to be higher for AW1 deflections and direction tuning sharpens further for AW2 deflections, while direction tuning diminishes in general after blockade of GABA receptors. In alignment with our results from the two barrel model, these observations emphasize the role of inhibition in generating direction tuning within the model – weaker responses are disproportionately suppressed by inhibition relative to stronger responses, and hence AW2 responses (in the intact network) are sculpted more by inhibition and exhibit sharper tuning than AW1 responses (or PW responses).

Finally, figure 8C examines the dynamics induced by a paired deflection protocol in which AW2 deflection precedes PW deflection, and shows the spiking response of a PW RS cell to the subsequent PW deflection and jitter in the timing of the first spike following PW deflection as functions of IDI. Due to the increased latency of the response to AW2 deflection relative to AW1 deflection, suppression of the subsequent PW deflection (in the intact network) begins at a larger IDI than in the case where the preceding deflection is of AW1 (compare left panels of figures 8C and 4A); bicuculline simulation, as expected, diminishes the suppressive effect of prior AW2 deflection (figure 8C-right). Figure 8C also shows that jitter tends to be highest for a middle range of IDIs during which prior AW2 deflection exhibits a partially suppressive effect on subsequent PW deflection (figure 8C-left). This may be due to a moderate level of fluctuating incoming inhibition for this middle range of IDIs causing high variability in the timing of the response to the subsequent PW deflection – for smaller IDIs, inhibition from prior AW2 deflection, due to its high latency, has not arrived prior to PW deflection, and spiking occurs immediately upon PW deflection and arrival of the ensuing excitation, yielding low jitter; for larger IDIs, inhibition from prior AW2 deflection arrives with full potency during PW deflection, sharply constraining the RS cell to be able to spike only at the peak of the incoming excitation induced by PW deflection (if it spikes at all), again resulting in low jitter. This effect is also seen in the case of bicuculline simulation (figure 8C-right), in which case it may be due to overlap of lingering excitation from prior AW2 deflection with excitation induced by subsequent PW deflection causing high fluctuations in net excitatory input and variable spike timing during this middle range of IDIs. For smaller IDIs, the high latency of AW2 dynamics ensures that excitation induced by PW

deflection arrives *prior* to excitation induced by AW2 deflection, with spiking occurring with a tight temporal lag upon PW deflection; for larger IDIs, excitation from prior AW2 deflection has likely dissipated, again causing spiking to occur with a tight temporal lag upon PW deflection and hence yielding lower jitter.

2.3 Discussion

In this work, we employ a modeling approach to examine the generation of multiwhisker receptive fields within the rat barrel cortex. Of the three possible mechanisms underlying the existence of multiwhisker responses – (i) inheritance of multiwhisker responses from TC cells in the aligned barreloid, (ii) direct input from AW barreloids, and (iii) lateral input from AW barrels – we specifically focus on the third hypothesis, and attempt to isolate the dynamics that lateral barrel-to-barrel connections entail by incorporating such lateral connections into our model while restricting TC cells to be responsive only to their PW and confining TC→RS connections to their PW-aligned barrel. Since experimental elucidation of the details pertaining to the nature, architecture, and dynamics of lateral barrel-to-barrel synapses is sparse (though see *Model Connectivity* and *Model Equations* subsections of the *Methods* for a summary of available data), we impose minimal assumptions on our model relating to the nature of barrel-to-barrel synaptic connectivity and include only random wiring. However, we find that, even without specific architectural constraints, the model is capable of capturing a broad range of physiological observations relating to the dynamics of RS cell responses to AW deflections or paired deflections, PW and AW direction selectivity, and the effects of bicuculline on the system.

In prior work (Patel, 2019), we adopt a similar strategy in a modeling approach to examine hypothesis (i), and we find from our prior work and the present work that both hypotheses (i) and (iii) are capable of explaining a broad range of the physiological data available on the dynamics of multiwhisker receptive fields within barrels. However, there are some empirical observations that hypothesis (iii) appears to capture naturally but which pose difficulties for hypothesis (i) – namely, observations showing that as the physical distance between two whiskers on the mystacial pad increases, the response of an RS cell, within the barrel corresponding to one of the whiskers, to deflection of the other whisker exhibits increased latency and diminishing amplitude (Armstrong-James, Fox, and Das-Gupta, 1992; Brecht and Sakmann, 2002a; Zhu and Connors, 1999). While hypothesis (i) can capture such observations by imbuing a TC cell

with AW responses whose latency and magnitude depend on the distance of the AW from the PW of the TC cell on the mystacial pad, there is no evidence of the existence of such distance dependence of the AW responses of TC cells. Hypothesis (ii) also appears unlikely to be able to provide a plausible explanation for this data, as there is no clear manner in which divergent barreloid input can account for the prolonging of RS cell response latencies as distance on the mystacial pad from the AW to the PW increases. However, it is quite biologically plausible that, within the full expanse of barrel cortex, nearby barrels corresponding to nearby whiskers would be more densely interconnected than spatially distant barrels corresponding to distant whiskers, an arrangement from which the observed dynamics would naturally emerge (as in the present model).

Furthermore, there exist some data which neither hypothesis (i) nor hypothesis (iii) (nor hypothesis (ii)), in isolation, appear to be able to capture. Kwegyir-Afful et al., 2005 show that a brainstem lesion that abolishes the AW responses of TC cells, while leaving PW responses intact, has an intriguing effect on responses to PW deflection in the corresponding barrel – RS cell spiking responses change little while FS cell spiking responses more than double. It is difficult to envision how hypothesis (i) or (iii) alone could explain these observations; elimination of AW responses of TC cells in hypothesis (i) should have no impact on PW responses in the corresponding barrel (Patel, 2019), while hypothesis (iii) does not posit AW responses of TC cells to begin with. However, it is possible that a combination of hypotheses (i) and (iii) – i.e., the existence of functionally significant multiwhisker receptive fields of TC cells as well as substantial conveying of AW responsivity through lateral barrel-to-barrel transmission – could lead to dynamics capable of giving rise to these observations, suggesting that, biologically, multiple mechanisms may contribute to the generation of multiwhisker receptive fields within rat barrel cortex. A mixture of mechanisms may also be able to provide a partial explanation for the often contradictory nature of results reported in the literature (described in more detail in the *Introduction*); e.g., individual ablation studies which appear to provide strong evidence for one mechanism or the other (Goldreich, Kyriazi, and Simons, 1999; Roy, Bessaih, and Contreras, 2011; Fox et al., 2003; Fox, 1994).

While, to our knowledge, there exists little modeling work that directly addresses in detail the feasibility of lateral connections as being the source of multiwhisker receptive fields (as in the present study), there exist several models of various aspects of barrel cortex function in general. For example, Puccini, Compte, and Maravall, 2006 employ an integrate-and-fire model to

study the effect of whisker deflection frequency on direction selectivity, with PW direction selectivity arising as a consequence of direction dependence in the latency of excitatory inputs to barrel RS cells. In the present work, PW direction selectivity arises as a consequence of feed-forward TC→RS cell wiring being dependent on PW direction preference, though prior work (Patel, 2018b) explores how the incorporation of RS→RS synapses may be able to explain direction dependence in the latency of excitation to RS cells. Interestingly, Wilson et al., 2010 model a developmental process which may lead to the emergence of direction tuning maps in barrel cortex, with the learning rule implemented in the model leading to the emergence of lateral connections across layers II and III that are most efficacious when adjacent whiskers are deflected in similar directions. Other models examine broad features of thalamocortical response transformations and the dynamic balancing of excitation and inhibition in the barrel system (Sharp, Petersen, and Furber, 2014; Kyriazi and Simons, 1993); notably, the model of Sharp, Petersen, and Furber, 2014 includes lateral connections between supragranular layers of barrel cortex in order to show that the lateral spread of excitation through supragranular layers can lead to AW responses in granular layers, though the intricacies and consequences of such lateral connections are not explored in this work.

2.4 Methods

The study models two barreloid/barrel systems within the rat barrel cortex, corresponding to nearby whiskers on the mystacial pad, that are interconnected via lateral barrel-to-barrel synapses. A barreloid/barrel system is comprised of TC cells (the thalamic barreloid) and RS and FS cells (the barrel). A whisker deflection is simulated by exciting TC cells within the barreloid corresponding to the deflected whisker, which synapse onto excitatory RS and inhibitory FS cells within the corresponding barrel, with the barrel FS cells delivering feedforward inhibition to barrel RS cells. Lateral connections from one barreloid/barrel to another are mediated solely by RS→RS and RS→FS synapses. TC cells within a barreloid respond only to deflections of their PW, and hence AW responses of RS cells arise solely from lateral input. Synaptic connectivity within the model is random but fixed; within a barrel, connection probabilities are determined by cell type and direction preference, while connection probabilities for lateral synapses are based solely on cell type. This model represents a modification of a model employed in prior work (Patel, 2018b; Patel, 2018a; Patel, 2019).

2.4.1 Model Connectivity

As observed experimentally (Land, Buffer, and Yaskosky, 1995), a model barreloid consists of 240 TC cells, and since empirical observations show TC cell clustering by PW direction preference (Timofeeva et al., 2003), TC cells in the model are split into 8 PW direction groups of 30 cells each, with each group assigned a preferred PW deflection direction ($0^\circ, 45^\circ, 90^\circ, 135^\circ, 180^\circ, 225^\circ, 270^\circ, 315^\circ$). A model barrel consists of 100 FS cells and 160 RS cells (experimentally, a barrel is approximated to have <400 FS cells and ~ 3600 RS cells (Bruno and Simons, 2002; Keller and Carlson, 1999; Welker and Woolsey, 1974; Beaulieu, 1993; Kawaguchi and Kubota, 1993)). RS cells are split into 8 PW direction domains of 20 cells each (data suggest that RS cell PW direction domains are organized in a pinwheel structure (Kremer et al., 2011; Andermann and Moore, 2006)), with each RS PW direction domain corresponding to a TC PW direction group within a barreloid/barrel system.

Intrabarrel connectivity: Since FS cells have been shown to lack direction selectivity and respond strongly to all deflection directions (Lee and Simons, 2004; Simons and Carvell, 1989; Bruno and Simons, 2002), it is likely that TC input to FS cells is not direction selective (Swadlow and Gusev, 2002); hence, within a barreloid/barrel system we set a TC \rightarrow FS connection probability of 0.65 for all TC PW direction groups (Bruno and Simons, 2002). The model has an intrabarrel FS \rightarrow FS connection probability of 0.5 (FS \rightarrow FS synapses in the model serve only to curtail the stimulus-induced FS population response) and an intrabarrel FS \rightarrow RS connection probability of 1. Experiments show that an RS PW direction domain within a barrel has a horizontal span of $\sim 100 \mu\text{m}$ (Bruno et al., 2003; Bruno and Simons, 2002; Keller and Carlson, 1999) (with individual RS cell dendritic arbors spanning $\sim 200 \mu\text{m}$ (Lubke et al., 2000; Simons and Woolsey, 1984)), while a TC cell axon arborizes widely throughout the horizontal span of the full barrel (Jensen and Killackey, 1987), with the highest density of axon terminals within a $\sim 200 \mu\text{m}$ horizontal range (Jensen and Killackey, 1987; Arnold, Li, and Waters, 2001); the extensive overlap of TC cell axon terminals with RS cell dendritic arbors suggests that a TC cell makes widespread synaptic connections to RS cells throughout its corresponding barrel, though synaptic densities vary with RS PW direction domain. Experimentally, the TC \rightarrow RS connection probability has been estimated to be ~ 0.37 on average (with each RS cell receiving input from ~ 80 -90 TC cells) (Timofeeva et al., 2003; Bruno and Simons, 2002; Bruno and Sakmann, 2006), and while RS cells are known to receive input from TC cells varying in PW direction preference (Timofeeva

et al., 2003), experiments indicate that the likelihood of a TC→RS synapse varies considerably in a direction-dependent manner, with higher connection probabilities associated with greater alignment between TC and RS PW direction preferences (Bruno and Simons, 2002; Bruno et al., 2003; Furuta, Deschenes, and Kaneko, 2011). Thus, within the model TC→RS synapses within a barreloid/barrel system are direction specific (with respect to the PW), with the probability of a synapse varying with TC group-RS domain alignment. The connection probability for a TC PW direction group to an RS PW direction domain is set at 0.7,0.5,0.3,0.15,0.1 for TC group-RS domain alignments that differ by 0°,45°,90°,135°,180°, respectively (this leads to an average TC→RS connection probability of 0.35, with ~84 TC cells synapsing onto an RS cell).

Interbarrel connectivity: Since the majority of inhibitory inputs to a barrel are of intracolumnar origin (Schubert et al., 2003; Staiger et al., 2009), lateral inhibition is not included in the model, and FS cell efferents are confined to their home barrel. Intracortical excitation, however, has been observed to reach layer IV directly via horizontal connections between layer IV cells in adjacent columns, as well as indirectly through vertical intracolumnar synapses from layers that integrate transcolumar inputs (Fox et al., 2003; Staiger et al., 2016). Functionally, both methods serve to convey excitation to RS and FS cells from other barrels, and differences between direct versus indirect barrel-to-barrel input have yet to be quantified (Schubert, Kotter, and Staiger, 2007; Gottlieb and Keller, 1997); thus, within the model, all cortical excitation originating outside of a barrel is abstracted into one source: direct RS→RS and RS→FS input from RS cells in a neighboring barrel. Since there is no evidence that lateral connectivity is based on direction preference (Schubert, Kotter, and Staiger, 2007), and since PW and AW direction preferences of RS cells have been shown to be uncorrelated (Simons and Carvell, 1989; Le Cam et al., 2011; Patel, 2019), lateral RS→RS and RS→FS synapses within the model are random with fixed connection probabilities determined by cell type. Experimental studies have determined that RS cells receive roughly 20% as many excitatory synapses from an adjacent barrel as from their home barrel; within our model, lateral connection probabilities are set higher than this result would suggest in order to compensate for the significantly lower number of RS cells in a model barrel than in a biological barrel (Schubert et al., 2003; Bruno and Simons, 2002), with lateral RS→RS and RS→FS connection probabilities set at 0.7 and 0.4, respectively.

2.4.2 Model Equations

TC cells are not explicitly simulated (the times of stimulus-induced TC spikes are drawn from a distribution, as described below in the *Stimulus Modeling* section). The membrane potential of neuron k, j within a barreloid/barrel system is governed by a reduced dimensional integrate-and-fire model of a cortical cell:

$$\frac{dV^{k,j}}{dt} = -g(V^{k,j} - V_{\text{rest}}) + I^{k,j}(t), \quad (2.1)$$

where $k \in \{\text{fs}, \text{rs}\}$, while $j \in \{1, 2, \dots, 100\}$ for $k = \text{fs}$ and $j \in \{1, 2, \dots, 160\}$ for $k = \text{rs}$. $V^{k,j}$ is the non-dimensional membrane potential, $g = 0.05 \text{ ms}^{-1}$ is the leak conductance, and $I^{k,j}(t)$ is the synaptic current (in ms^{-1}). $V_{\text{rest}} = 0$ is the resting potential, and a spike is recorded when $V^{k,j} \rightarrow 1^-$, at which point $V^{k,j}$ is instantaneously reset to V_{rest} . A refractory period is simulated by holding $V^{k,j}$ at V_{rest} for 2 ms following a spike. The integrate-and-fire equation has a membrane time constant of 20 ms, consistent with the experimentally observed ~ 17 ms time constant of RS cells (Gabernet et al., 2005). Details of the reduced dimensional model are given in (Tao et al., 2004).

Intrabarrel dynamics: A spike of a neuron presynaptic to neuron k, j leads to a jump in $I^{k,j}(t)$ followed by exponential decay, after a manually imposed synaptic latency. Let $n^{k,j}$ denote the total number of presynaptic spikes that impinged upon neuron k, j during a trial. If the r^{th} presynaptic spike occurs at time $t_r^{k,j}$, and $m \in \{\text{tc}, \text{fs}\}$ is the type of the presynaptic neuron, the current $I^{k,j}(t)$ induced in neuron k, j at time t is given by the following:

$$i_r^{k,j}(t) = \begin{cases} 0 & t < t_r^{k,j} + d_m^k \\ A_m^k e^{-\alpha_m^k(t - t_r^{k,j} - d_m^k)} & t \geq t_r^{k,j} + d_m^k \end{cases} \quad (2.2)$$

$$I^{k,j}(t) = \sum_{r=1}^{n^{k,j}} i_r^{k,j}(t). \quad (2.3)$$

d_m^k denotes the synaptic delay, α_m^k dictates the decay rate, and A_m^k indicates the amplitude of an input from a neuron of type $m \in \{\text{tc}, \text{fs}\}$ to a neuron of type $k \in \{\text{fs}, \text{rs}\}$. For the synaptic delay, $d_{\text{tc}}^{\text{fs}} = 0, d_{\text{tc}}^{\text{rs}} = 0, d_{\text{fs}}^{\text{fs}} = 0, d_{\text{fs}}^{\text{rs}} = 3$ ms. We introduced the delay parameter to match the experimental observation that a TC spike leads to an EPSP in the RS cell followed by an IPSP with a several ms time lag (Gabernet et al., 2005), though the delay parameter does not qualitatively

affect the dynamics of the model (due to model architecture, TC-induced FS spiking and TC-induced RS spiking must precede FS→RS and RS→RS input, respectively, ensuring that FS and RS input to an RS cell is delayed relative to TC input). For the decay rate, $\alpha_{tc}^{fs} = 0.73, \alpha_{tc}^{rs} = 0.75, \alpha_{fs}^{fs} = 0.18, \alpha_{fs}^{rs} = 0.18 \text{ ms}^{-1}$. We chose these values to approximately match experimental data showing that TC synapses are fast and decay over a $\sim 1\text{-}2$ ms time scale, while FS synapses are slightly slower and decay over a $\sim 5\text{-}6$ ms time scale (Gabernet et al., 2005). The exact values of the decay rates (so long as synapses are fast, within the range of a few milliseconds) do not qualitatively affect model dynamics. For the amplitude, $A_{tc}^{fs} = 0.3, A_{tc}^{rs} = 0.04, A_{fs}^{fs} = 0.1, A_{fs}^{rs} = 0.03 \text{ ms}^{-1}$. We chose the amplitude parameters for approximate agreement with the following experimental observations on synaptic strengths within a barreloid/barrel system: 1) TC→RS synapses are relatively weak in comparison to potent TC→FS synapses (~ 30 incoming TC spikes are required to elicit a spike in an RS cell, while a few incoming TC spikes are capable of eliciting a spike in an FS cell) (Gabernet et al., 2005; Temereanca, Brown, and Simons, 2008); 2) TC spikes elicit a $\sim 4\text{-}8$ fold larger EPSP in an FS cell than in an RS cell (Cruikshank, Lewis, and Connors, 2007); 3) the postsynaptic current in an RS cell induced by a whisker deflection is dominated by inhibition (in an RS cell, the ratio $\frac{\text{EPSC}}{\text{EPSC} + \text{IPSC}} = \sim 0.2$) (Gabernet et al., 2005).

Interbarrel dynamics: The same set of equations is used to model lateral synapses; in this case, $d_m^k, \alpha_m^k,$ and A_m^k denote inputs from a neuron of type $m \in \{\text{rs}\}$ to a neuron of type $k \in \{\text{fs}, \text{rs}\}$. Decay is set to $\alpha_{rs}^{rs} = \alpha_{rs}^{fs} = 0.24 \text{ ms}^{-1}$, synaptic delay is set to $d_{rs}^{rs} = d_{rs}^{fs} = 2 \text{ ms}$, and amplitude is set at a default of $A_{rs}^{rs} = 0.006, A_{rs}^{fs} = 0.08 \text{ ms}^{-1}$. Empirically, AW responses are observed to show lower spike counts and longer latencies relative to PW responses (Brecht and Sakmann, 2002a; Simons and Carvell, 1989; Fox, 2018). The delay parameter within our model captures the experimental observation that AW responses exhibit ~ 2 ms longer latencies than PW responses (Simons, 1985; Simons and Carvell, 1989). Likewise, amplitude parameters were determined based on studies showing that excitation from an adjacent barrel is more than 75% weaker than excitation from the home barrel (with somewhat high variance), and spike counts yielded by AW deflections are between 40 – 80% for FS cells and 20 – 60% for RS cells of spike counts resulting from PW deflections (Schubert et al., 2003; Fox et al., 2003; Kyriazi and Simons, 1993; Bruno and Simons, 2002; Armstrong-James, Fox, and Das-Gupta, 1992).

2.4.3 Stimulus Modeling

Experimental data indicate that a whisker deflection tends to elicit at most one spike in a TC cell within its corresponding barreloid (Pinto, Brumberg, and Simons, 2000). Hence, in order to simulate a whisker deflection, we assign spike probabilities to TC cells within the corresponding barreloid (each TC cell spikes either 0 or 1 times), and we draw spike times for those TC cells that spike from an inverse Gaussian distribution with a standard deviation of 1 ms. The inverse Gaussian distribution is the most concordant in shape with experimentally measured TC spike time distributions (Pinto, Brumberg, and Simons, 2000)).

Experimental data indicate that TC cells are clustered into groups by PW direction preference (Timofeeva et al., 2003), and that as the direction of a PW deflection deviates away from the preferred direction of a TC direction group, the magnitude of the group's response diminishes, though the synchrony (i.e., spike time distribution) of the TC group's response does not change appreciably (Pinto, Brumberg, and Simons, 2000; Temereanca and Simons, 2003). To simulate the encoding of deflection direction by TC response magnitude, we set the TC spike probability within a given direction group (in the model barreloid corresponding to the deflected whisker) at 0.8, 0.7, 0.4, 0.15, 0.1 to simulate a deflection at a direction of 0° , 45° , 90° , 135° , 180° , respectively, away from the preferred PW deflection direction of the TC direction group; TC spike probabilities within the barreloid not corresponding to the deflected whisker are set at 0. This yields a PW tuning ratio (response to preferred direction/average response over all directions) of 1.86 for individual TC cells, concordant with experiment (Bruno and Simons, 2002). Thus, to simulate a deflection of a particular whisker at time t^* at a particular angular direction, each TC cell within the barreloid corresponding to the whisker is set to spike either 0 or 1 times; TC spike times (for those TC cells that spike) are drawn from an inverse Gaussian distribution centered at time t^* , with deflection direction determining the probability that a TC cell in each direction group emits a spike.

2.4.4 Simulation and Data Analysis

Data presented in manuscript figures are averaged over 50 or 100 trials. For a fixed stimulus, spikes per deflection is calculated as total number of spikes over all trials/number of trials. Experiments indicate that the spike response of an RS cell to a preferred stimulus (if the cell responds at all) is low, with reported mean response values of 0.88 spikes/stimulus (Wilent and

Contreras, 2005), 1.14 spikes/stimulus (Lee and Simons, 2004), 1.3 spikes/stimulus (Bruno and Simons, 2002), or 1-2 spikes/stimulus (Pinto, Brumberg, and Simons, 2000). Accordingly, within the model RS cells tend to spike at most once or twice per trial, with the majority spiking only once.

A direction tuning curve for an RS cell is obtained by calculating the spike response of the RS cell for each deflection direction ($0^\circ, 45^\circ, 90^\circ, 135^\circ, 180^\circ, 225^\circ, 270^\circ, 315^\circ$). The spike response of the RS cell for a fixed deflection direction is calculated as spikes per deflection averaged over 100 deflection trials. The preferred direction of the RS cell is defined as the single deflection direction that yields the maximum spike response. Spike responses of the RS cell for directions equidistant from preferred are averaged together (e.g., for an RS cell with 0° direction preference, spike responses for 45° and 315° deflections are averaged, spike responses from 90° and 270° deflections are averaged, and spike responses from 135° and 225° deflections are averaged); the direction tuning curve of the RS cell is plotted as the spike response of the RS cell as a function of the angular distance of whisker deflection direction from preferred. The direction tuning ratio of the RS cell is calculated as follows: spike response to preferred direction/mean spike response over all deflection directions.

Means, standard deviations, and correlations are calculated using Python's statistics module. Simulations are carried out using Euler's method with a time step of 0.01 ms. Model code is freely available at <https://github.com/lma000/LateralBarrelModel>.

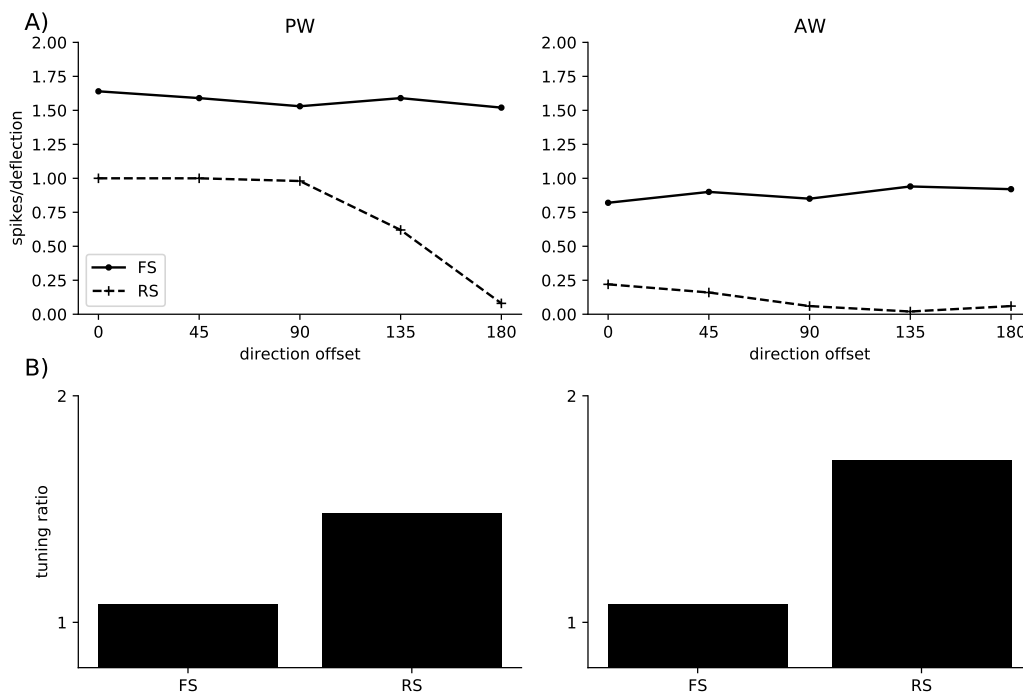


Figure S1. Lack of direction selectivity in FS cells in response to both PW (left) and AW (right) deflections. Comparisons of tuning curves for single FS and RS cells are plotted in A), and tuning ratios for the same cells are plotted in B). Data are gathered over 50 trials.

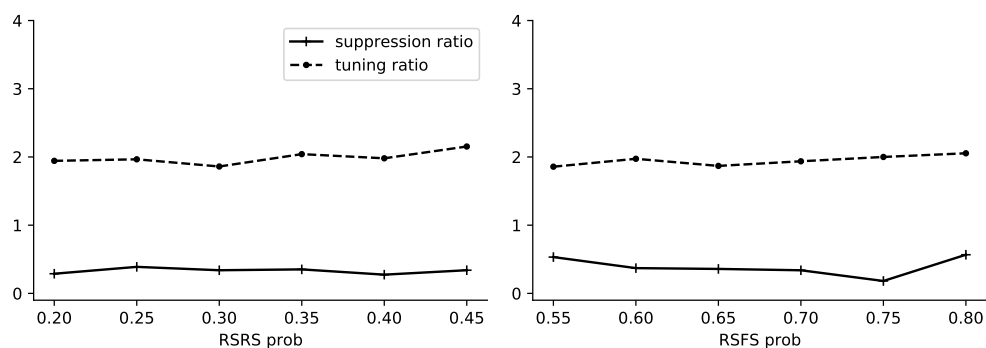


Figure S2. Diminished changes in response to changing the synaptic density of lateral connections between the PW and AW barrel for RS→RS (left) and RS→FS synapses, while keeping synaptic amplitudes fixed, on suppression ratios and AW tuning ratios of RS cells within the PW barrel. Tuning ratio is calculated for single AW whisker deflections as response to preferred direction/average response over all directions; suppression ratio is calculated for paired deflections as ((response to PW alone - response to PW after prior AW deflection)/response to PW alone). Data are averaged over all RS cells in the PW barrel. For paired whisker deflections, AW deflection angle is set at 0° , PW deflection angle is set at the preferred PW direction of the cell, and interdeflection interval is set to 8.5 ms.

Chapter 3

γ Frequency Oscillations in the CA3 ¹

Abstract

Gamma oscillations are a prominent feature of various neural systems, including the CA3 subfield of the hippocampus. In CA3, in vitro carbachol application induces ~ 40 Hz gamma oscillations in the network of glutamatergic excitatory pyramidal neurons (PNs) and local GABAergic inhibitory neurons (INs). Activation of NMDA receptors within CA3 leads to an increase in the frequency of carbachol-induced oscillations to ~ 60 Hz, a broadening of the distribution of individual oscillation cycle frequencies, and a decrease in the time lag between PN and IN spike bursts. In this work, we develop a biophysical integrate-and-fire model of the CA3 subfield, we show that the dynamics of our model are in concordance with physiological observations, and we provide computational support for the hypothesis that the 'E-I' mechanism is responsible for the emergence of ~ 40 Hz gamma oscillations in the absence of NMDA activation. We then incorporate NMDA receptors into our CA3 model, and we show that our model exhibits the increase in gamma oscillation frequency, broadening of the cycle frequency distribution, and decrease in the time lag between PN and IN spike bursts observed experimentally. Remarkably, we find an inverse relationship in our model between the net NMDA current delivered to PNs and INs in an oscillation cycle and cycle frequency. Furthermore, we find a disparate effect of NMDA receptors on PNs versus INs – we show that NMDA receptors on INs tend to increase oscillation frequency, while NMDA receptors on PNs tend to slightly decrease or not affect oscillation frequency. We find that these observations can be explained if NMDA activity above a threshold level causes a shift in the mechanism underlying gamma oscillations; in the absence of NMDA

¹Ma, L. & Patel, M. Mechanism of carbachol-induced 40 Hz gamma oscillations and the effects of NMDA activation on oscillatory dynamics in a model of the CA3 subfield of the hippocampus. Submitted. L.M. implemented the model, analyzed the data, and drafted the manuscript. M.P. designed the study and revised the manuscript.

receptors, the 'E-I' mechanism is primarily responsible for the generation of gamma oscillations (at 40 Hz), while when NMDA receptors are active, the mechanism of gamma oscillations shifts to the 'I-I' mechanism, and we argue that within the 'I-I' regime (which displays a higher baseline oscillation frequency of ~ 60 Hz), slight changes in the level of NMDA activity are inversely related to cycle frequency.

3.1 Introduction

Network oscillations are a ubiquitous phenomenon within the nervous system (Steriade, 2006; Patel and Joshi, 2015; Gregoriou, Paneri, and Sapountzis, 2015; Courtemanche, Robinson, and Aponte, 2013; Patel, Rangan, and Cai, 2009; Patel, Rangan, and Cai, 2013; Colgin, 2011; Rybak et al., 2004; Buzsaki and Draguhn, 2004), and gamma oscillations are defined as rhythmic network activity within the 30-90 Hz range (Buzsaki, and Wang, 2012). Gamma oscillations are a prominent feature of the hippocampal system, and are thought to play a crucial role in information processing within the hippocampus and in communication between the hippocampus and other cortical structures (Harris and Gordon, 2015; Hanslmayr, Staerensina, and Bowman, 2016; Draguhn, Keller, and Reichinnek, 2014; Lisman and Jensen, 2013; Colgin and Moser, 2010; Axmacher et al., 2006). Experimental evidence suggests that, within the hippocampus, gamma oscillations are generated within the CA3 subfield and subsequently propagate from CA3 to other subregions (Zemankovics et al., 2013).

The CA3 subfield consists of excitatory glutamatergic pyramidal neurons (PNs), which provide the sole output of CA3 in the form of Schaffer collaterals (Witter, 2007), along with several classes of GABAergic interneurons (INs), which provide local inhibition within CA3 (Bartos, Alle, and Vida, 2011). PN and IN synapses display fast kinetics (Bartos et al., 2002; Bartos, Alle, and Vida, 2011), and CA3 exhibits a feedforward inhibitory structure – mossy fibers from the dentate gyrus and perforant path input from the entorhinal cortex excite both CA3 PNs and INs (Witter, 2007; Lawrence and McBain, 2003), an arrangement which implies that PNs receive monosynaptic excitation (from mossy fibers and the perforant path) followed by disynaptic inhibition from INs, with a small time lag between excitation and inhibition arising due to the time scale of IN activation by mossy fiber/perforant path input and the synaptic delay in IN to PN synapses. Such a feedforward inhibitory structure is present in numerous neural systems and has been studied extensively (Mittmann, Koch, and Häusser, 2005; Fricker and Miles, 2000;

Wehr and Zador, 2003; Blitz and Regehr, 2005; Jortner, Farivar, and Laurent, 2007; Patel and Reed, 2013), and prior work has shown that such a feedforward arrangement results in PNs that respond selectively to synchrony in the external excitation impinging upon them (Patel and Joshi, 2013; Joshi and Patel, 2013; Liu, Patel, and Joshi, 2014).

Within CA3, however, this purely feedforward structure is augmented by the presence of PN feedback, since a significant number of recurrent PN collaterals are routed back into CA3 to form synaptic contacts with INs (figure 3.1) (Gulyas et al., 1993; Sik, Tamamaki, and Freund, 1993; Wittner et al., 2006). The presence of recurrent PN collaterals endows CA3 with the ability to generate intrinsic gamma oscillations – external excitation elicits a synchronous burst of PN activity, which results in PN collaterals feeding back to elicit a prolific burst of IN spikes, which in turn suppresses PNs for a brief time, and once inhibition subsides a burst of PN spikes ensues, beginning the cycle anew and resulting in a sustained network oscillation so long as the external excitatory input endures. In vitro, network gamma oscillations within the ~ 40 Hz range can be induced cholinergically within the CA3 subfield (Zemankovics et al., 2013; Fisahn et al., 1998; Mann et al., 2005; Hajos et al., 2004), and evidence shows that infusion of either a GABA_A receptor antagonist or an AMPA receptor antagonist abolishes the intrinsic oscillatory activity of the CA3 network (Mann et al., 2005; Fisahn et al., 1998), indicating that the mechanism underlying the CA3 network gamma oscillation relies crucially on both IN inhibition as well as PN excitation.

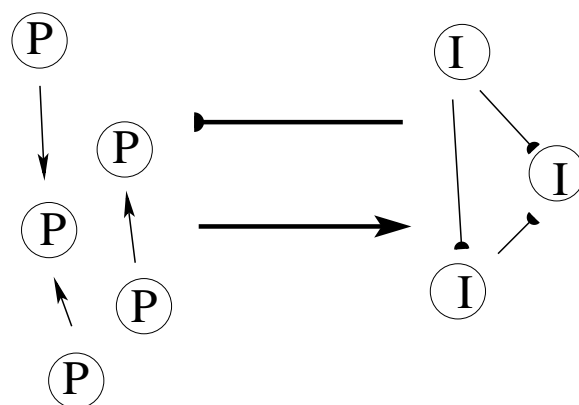


Figure 3.1. Schematic of the CA3 network. Arrow heads indicate excitation, while bar heads indicate inhibition. PNs excite each other and supply recurrent excitation to INs. INs inhibit each other and inhibit PNs. External cholinergic input (not shown) induces gamma oscillations.

In addition to acting through fast synapses mediated by AMPA and GABA_A receptors, CA3

PNs also exert local excitatory influence through slower NMDA receptors (Bartos, Alle, and Vida, 2011; Mann and Paulsen, 2007; Lawrence and McBain, 2003; Bartos et al., 2002). However, evidence indicates that NMDA receptors play little role in the cholinergically induced ~ 40 Hz gamma oscillations observed in CA3 in vitro, as NMDA blockade has no impact on this rhythmic activity (Fisahn et al., 1998; Mann et al., 2005). Under normal circumstances, tonic inhibition mediated by extrasynaptic δ -GABA_A receptors prevents activation of NMDA receptors, presumably due to the voltage-dependent NMDA block, while in mice in which δ -GABA_A receptors have been knocked out NMDA receptors are able to activate, yielding a rise in the gamma oscillation frequency to ~ 60 Hz. The activation of NMDA receptors results in a broadening of the frequency distribution of oscillation cycles and a right-shift in the peak of the distribution, as well as yielding a diminished time lag between excitatory PN and inhibitory IN spike bursts during a gamma oscillation cycle, suggesting that NMDA activation may cause a shift in the physiological mechanism underlying the generation of network oscillations (Mann and Mody, 2010).

In this work, we develop a biophysical integrate-and-fire network model of the CA3 sub-field, with model parameters constrained by physiological data, and examine the mechanism underlying the emergence of carbachol-induced ~ 40 Hz gamma oscillations within the model. Furthermore, we incorporate NMDA receptors into the model, and we study the increase in gamma oscillation frequency, broadening of the cycle frequency distribution, and diminishing time lag between PN and IN spike bursts resulting from NMDA activation. Finally, we study the shift in the mechanism of gamma oscillation generation in our model with the introduction of NMDA receptors, and we propose a physiologically based explanation of the effect of NMDA activation and the ensuing shift in the oscillatory dynamics of the CA3 network.

3.2 Results

The CA3 model consists of 200 PNs and 50 INs, with the membrane potential of each neuron modeled by an integrate-and-fire equation. Synaptic connections among neurons within the model are random but fixed with cell-type specific connection probabilities – PNs excite each other as well as excite INs through fast AMPA-mediated synapses, and INs inhibit each other as well as inhibit PNs through fast GABA_A-mediated synapses (figure 3.1). PNs also exert excitatory synaptic influence on postsynaptic cells through slower NMDA receptors, and we examine

network behavior in the presence and absence of NMDA receptors. In vitro, external cholinergic input to PNs and INs is employed to induce gamma oscillations (Zemankovics et al., 2013; Fisahn et al., 1998; Mann et al., 2005; Hajos et al., 2004) – in our model, external cholinergic input is simulated as a small white noise current to PNs and INs within the network. Model details and experimental justification of model parameters are provided in the Methods.

3.2.1 Network Behavior Without NMDA

Figure 2 summarizes network spiking behavior in the absence of NMDA receptors. Without NMDA, the simulated external cholinergic input induces oscillatory spiking in the PN and IN populations; as shown in the spike rasters in figure 3.2A, a burst of PN and IN spikes occurs approximately every 25 ms, with the subset of PNs or INs that contribute spikes to each burst changing from one oscillation cycle to the next. Thus, while the aggregate PN or IN populations spike every ~ 25 ms, an individual PN or IN spikes only during a fraction of available oscillation cycles. This is apparent in the mean firing rates shown in figure 3.2B – the mean firing rate of PNs within our network is 6.1 ± 1.79 Hz (indicating that an individual PN spikes only during a small fraction of oscillation cycles), while the mean firing rate of INs within the network is 40.76 ± 9.52 Hz (indicating that an individual IN tends to spike on most oscillation cycles). This is in accordance with experimentally measured PN and IN activity (Hajos et al., 2004; Hajos and Paulsen, 2009; Oren et al., 2006). The aggregate spiking behavior of the PN and IN populations is depicted in figure 3.2C, in which the total number of PN and IN spikes is plotted as a function of time, showing that the PN and IN populations both exhibit oscillatory spiking, with the peak in IN spikes lagging behind the peak in PN spikes with an average time difference of 3.0 ± 0.70 ms, in approximate accordance with experiment (Zemankovics et al., 2013; Mann et al., 2005). Figure 3.3B (bottom panel) depicts the distribution of the location of the cycle peak in PN or IN activity (with oscillation cycles placed on a 2π scale), showing a tendency for a phase lag between peaks in PN and IN activity. The time or phase difference in PN and IN spiking apparent from figures 3.2C or 3.3B (bottom panel) is suggestive of a causal relationship – i.e., that a PN spike burst is crucial in exciting INs and eliciting an IN spike burst.

Figure 3.3A (top) shows the local field potential (LFP) of the network, calculated as the average membrane potential of all neurons within the network, and suggests a strong tendency for neurons within the network to exhibit synchronized oscillations in membrane potential. The bottom panel of figure 3.3A shows the power spectrum of the LFP, indicating a clear 40 Hz peak

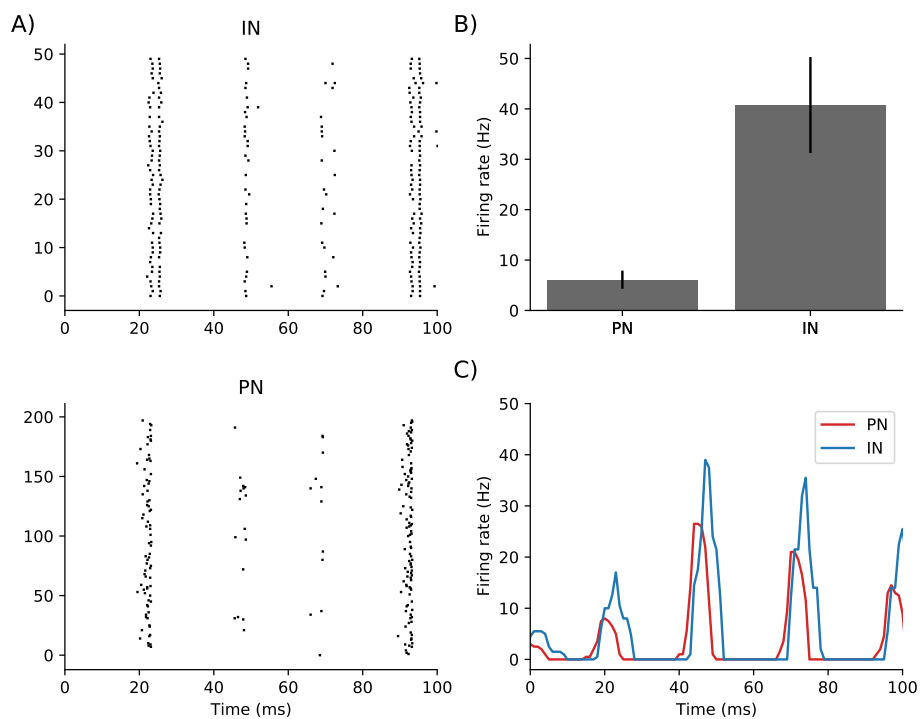


Figure 3.2. Model firing rates in the absence of NMDA receptors. A) Spike rasters for INs (top) and PNs (bottom) over 100 ms of network activity. B) Firing rate of a model PN or IN, measured over 1600 ms of network activity. Mean firing rate of PNs and INs within the network are 6.1 ± 1.79 Hz and 40.76 ± 9.52 Hz, respectively. Data is averaged over all PNs or all INs in the network; error bars represent standard deviation. C) Population firing rates of network PNs and INs, measured in 5 ms bins with a 1 ms sliding window. Time difference between PN and IN peaks: 3.0 ± 0.70 ms.

(or a ~ 25 ms oscillation period), as observed *in vitro* during carbachol-induced oscillations (Zemankovics et al., 2013; Fisahn et al., 1998; Mann et al., 2005; Hajos et al., 2004). The separated PN and IN field potentials in figure 3.3B (top) (calculated as the average membrane potential of all PNs and INs in the network, respectively), similar to the aggregate spiking behavior in figure 3.2C, shows that oscillations in the IN field potential exhibit a small time lag in relation to PN field potential oscillations, again suggestive of a causal relationship. Furthermore, figure 3.3B (top) shows that the PN field potential exhibits large, robust oscillations with troughs dipping well below the resting potential of 0, while the IN field potential exhibits smaller oscillations and remains mostly above the resting potential. This suggests that oscillations in the PN field potential are controlled by inhibition – troughs in the PN field potential can only be due to potent, synchronized inhibition arriving from the IN population, with external excitation (simulating carbachol application) allowing PN membrane potentials to climb to threshold once the inhibition subsides. Oscillations in the IN field potential, however, appear to be controlled more by

PN activity rather than by IN inhibition; since the IN field potential remains approximately constant and near the resting potential, except for upward swings following peaks in the PN field potential, it is likely that external excitation (i.e., carbachol application) is insufficient to bring IN membrane potentials to threshold, and that these upward swings (and presumably, IN spikes) are due primarily to phasic excitation arriving from PNs, rather than to a relenting of inhibition from other INs.

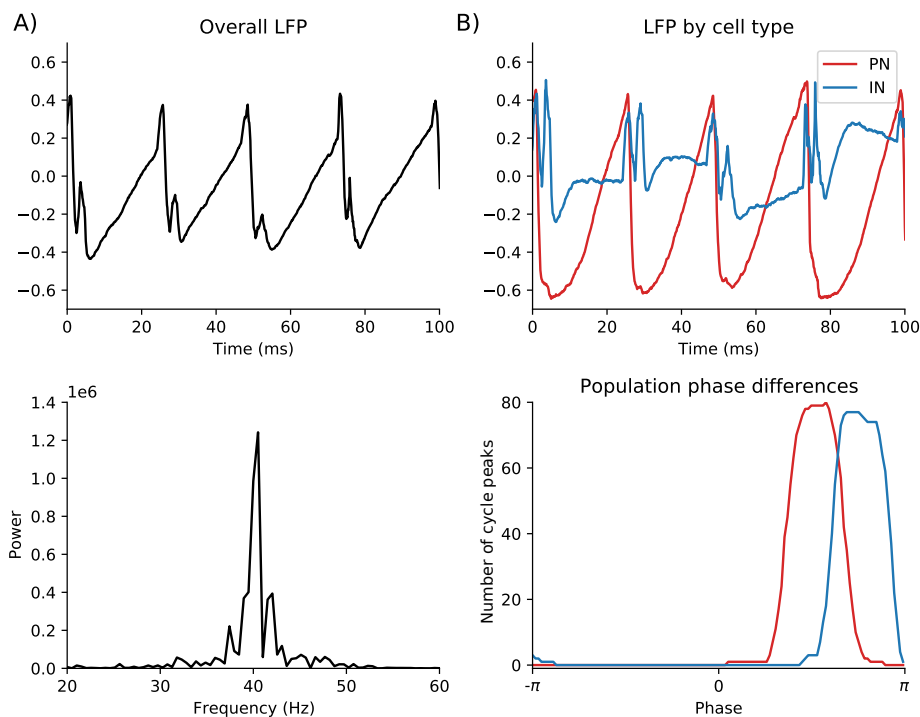


Figure 3.3. Oscillatory properties of the model in the absence of NMDA receptors. A) Top: Local field potential (LFP) of the model, computed as the average membrane potential of all neurons within the network. Bottom: Power spectrum of the LFP in the top panel. B) Top: LFP by cell type, computed as the average membrane potential of all PNs or all INs within the network. Bottom: Location of the peak in PN and IN population firing rates during an oscillation cycle, with cycle period represented on a 2π scale. Data are collected for a total of 67 oscillation cycles; y-axis shows the number of oscillation cycles for which the peak in PN or IN activity occurred at each cycle location on the x-axis. Data are binned in $\frac{\pi}{4}$ windows with a sliding step size of $\frac{\pi}{100}$.

This interpretation is supported by the nature of inputs to individual neurons within the network, as depicted in figure 3.4. Figure 3.4A shows the membrane potential and AMPA-mediated and GABA_A-mediated input current for a sample PN and IN within the network; input to the PN is dominated by inhibition, with troughs in membrane potential oscillations reliably following

inhibitory input, while input to the IN exhibits a significant level of synaptic excitation, with upward swings in the membrane potential of the IN coinciding with incoming excitation. Figure 3.4B (bottom) shows the inhibitory and excitatory input to a sample PN and IN in an oscillation cycle (averaged over multiple cycles), while figure 3.4B (top) shows the average inhibitory and excitatory input to all PNs and all INs in a sample oscillation cycle. Figure 3.4B shows that, in accordance with experiment (Zemankovics et al., 2013; Oren et al., 2006; Hajos and Paulsen, 2009) and with the above interpretation, input to PNs, on average, is dominated by inhibition from INs (as opposed to excitation from other PNs), while input to INs, on average, exhibits a relatively heavier influence from synaptic excitation delivered by PNs.

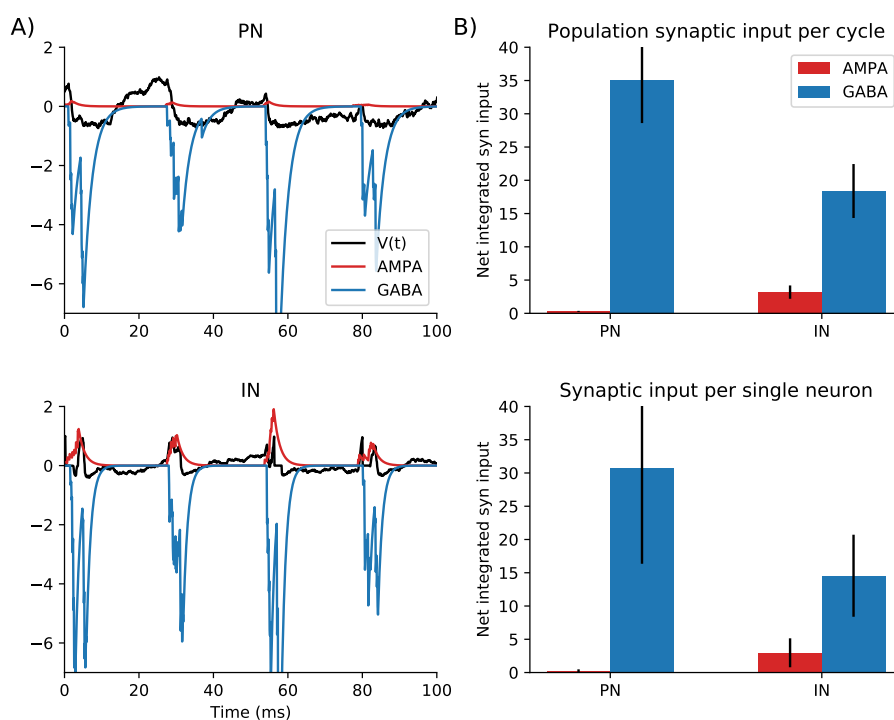


Figure 3.4. Model synaptic inputs in the absence of NMDA receptors. A) Membrane potential, net excitatory synaptic input through AMPA receptors, and net inhibitory GABAergic input to a single representative PN (top) or IN (bottom) in the network. B) Top: Net excitatory or inhibitory synaptic input to a PN or IN during an oscillation cycle; data are collected during a fixed oscillation cycle and averaged over all PNs or INs within the network. Bottom: Net excitatory or inhibitory synaptic input to a PN or IN during an oscillation cycle; data are collected for a single PN or IN and averaged over 67 oscillation cycles. Net excitatory or inhibitory input to a cell during a cycle is computed via numerical integration. Error bars represent standard deviation.

Thus, our model predicts that *in vitro* CA3 gamma oscillations are dependent on PN feedback to INs. The external excitation to neurons within our model (simulating *in vitro* carbachol

application) is sufficient to bring PNs to threshold, but not strong enough to bring INs to threshold. The INs within our model (without PN input) spike only sporadically and tend to equilibrate at a membrane potential that is, on average, below threshold. The PNs within our model (without IN input) tend to spike continuously; in this scenario, PN spikes elicit spikes from the otherwise quiescent INs, which in turn suppress PN activity. Connectivity among PNs and INs tends to synchronize the activity of these two subpopulations (connectivity among PNs tends to ensure that multiple PNs spike simultaneously, while connectivity among INs tends to ensure that a burst of IN spikes delays the next possible burst of IN spikes), and network dynamics are quickly organized into an oscillatory regime – a PN spike burst elicits an IN spike burst, which in turn suppresses PNs, and once the inhibition subsides another PN spike burst begins the cycle anew. Since INs must wait for PN input prior to spiking, there is a significant time delay (3.0 ± 0.70 ms, figure 3.2C) between PN and IN spike bursts. Furthermore, for oscillations to occur, IN input to PNs must be strong (in order to efficaciously suppress PN activity for a short time period after an IN spike burst) and PN input to INs must be strong (in order to effectively elicit an IN spike burst following a PN spike burst), as shown in figure 3.4. This is consistent with the ‘E-I’ mechanism of hippocampal CA3 gamma oscillations proposed by (Fisahn et al., 1998; Mann et al., 2005) (discussed in the next subsection). The ~ 25 ms period of the oscillation in our network is determined by the time scales of synaptic dynamics; the latency and time course of synaptic excitation from PNs to INs (as well the time course of the IN membrane response) and the latency and time course of synaptic inhibition from INs to PNs (as well as the time course of the PN membrane response) lead to the aggregate time scale for the network oscillation.

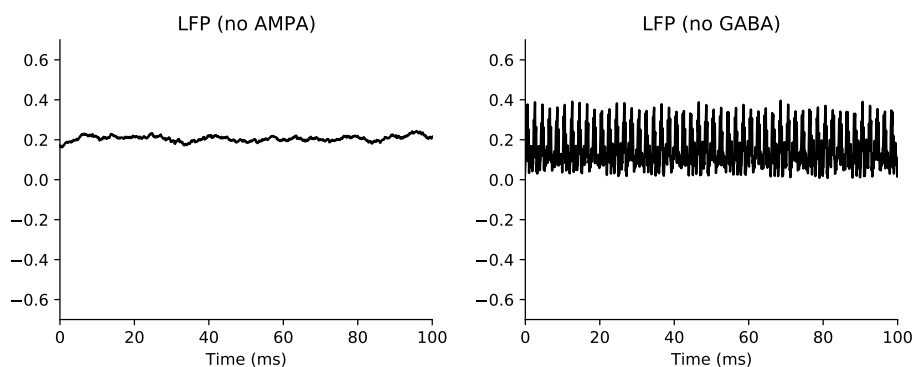


Figure 3.5. Local field potential of the model in the absence of NMDA receptors, computed as the average membrane potential of all cells within the network, following removal of excitation (left) or inhibition (right) from the network.

Further support for this hypothesis is provided in figure 3.5 – figures 3.5 (left) and figure 3.5 (right) show the local field potential of our model network after severing AMPA or GABA_A synapses, respectively, showing that gamma oscillations vanish after blockade of either of these receptors (consistent with in vitro experimental results after application of an AMPA or GABA_A antagonist (Mann et al., 2005; Fisahn et al., 1998)). Without AMPA synapses, PN input to INs is eliminated, and figure 3.5 (left) suggests that without PN input the IN population is unable to coalesce its activity into robust spike bursts (though sporadic IN spiking may still occur), and hence no influence within the network exists that is capable of synchronizing PN spiking activity. Without GABA_A synapses, the lack of inhibition to PNs leads to frequent but unsynchronized PN spiking, which likely causes frequent but unsynchronized IN spiking (as there are no IN-IN synapses to organize IN activity).

3.2.2 Network Behavior With NMDA

In vitro experimental evidence indicates that activation of NMDA receptors in the CA3 subfield leads to a general increase in the frequency of carbachol-induced gamma oscillations, along with a wider distribution in the instantaneous frequency of individual oscillation cycles, as well as a decrease in the time lag between (i.e., increase in the synchrony of) PN and IN spike bursts (Mann and Mody, 2010). In order to study this phenomenon, we included NMDA receptors in our CA3 model, with NMDA synapses distributed in an identical manner to AMPA synapses. Experimental evidence suggests that NMDA synapses are found on both PNs and INs, though differing subtypes may be present on the two classes of cells (Mann and Mody, 2010; Brandalise et al., 2016; Berg et al., 2013), and we therefore include NMDA receptors on both PNs and INs in our model. Details of NMDA receptor dynamics in our model are provided in the Methods.

Figure 3.6 summarizes network behavior in the presence of NMDA receptors. Figure 3.6A shows mean PN and IN firing rates in the presence of NMDA receptors, while the aggregate spiking behavior of the PN and IN populations (the total number of PN and IN spikes as a function of time) is depicted in figure 3.6D. Figure 3.6D shows that the PN and IN populations both exhibit oscillatory spiking, with peaks in IN spikes exhibiting a mean time lag of 1.29 ± 2.84 ms behind peaks in PN spikes – the time lag between PN and IN spike peaks decreases (from 3.0 ± 0.70 ms in the absence of NMDA receptors) with NMDA activation, as observed experimentally (Mann and Mody, 2010). Figure 3.6B shows the local field potential of the network, and the power spectrum of the LFP (figure 3.6C) shows diminished oscillatory power but a right-shift in the peak

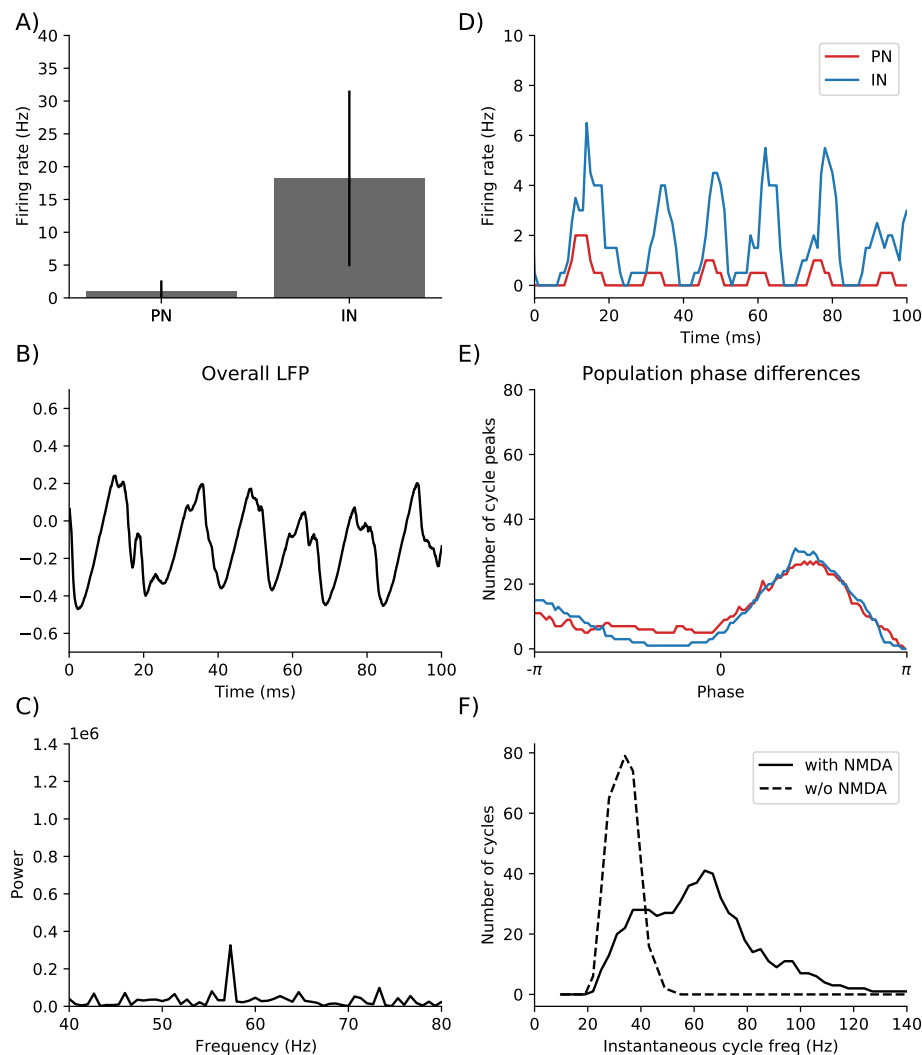


Figure 3.6. Model firing rates and oscillatory properties with active NMDA receptors. A) Firing rate of a model PN or IN, measured over 1600 ms of network activity. Mean firing rate of PNs and INs within the network are 1.00 ± 1.65 Hz and 18.21 ± 13.39 Hz, respectively. Data is averaged over all PNs or all INs within the network; error bars represent standard deviation. B) Model LFP, computed as the average membrane potential of all cells within the network. C) Power spectrum of the LFP shown in B). D) Population firing rates of network PNs and INs, measured in 5 ms bins with a 1 ms sliding window. Time difference between PN and IN peaks: 1.29 ± 2.84 ms. E) Location of the peak in PN and IN population firing rates during an oscillation cycle, with cycle period represented on a 2π scale. Data are collected for a total of 67 oscillation cycles; y-axis shows the number of oscillation cycles for which the peak in PN or IN activity occurred at each cycle location on the x-axis. Data are binned in $\frac{\pi}{4}$ windows with a sliding step size of $\frac{\pi}{100}$. F) Distribution of instantaneous cycle frequency, in the case of either active or absent NMDA receptors. Data points represent number of cycles within 15 Hz bins, using a 1 Hz sliding window; a total of 67 cycles were collected for each of the two cases.

frequency of LFP oscillations, compared to the case with inactive NMDA receptors shown in figure 3.3A (Mann and Mody, 2010). Figure 3.6E depicts the distribution of the location of the

cycle peak in PN or IN activity (with oscillation cycles placed on a 2π scale), showing a tendency for a decrease in phase lag and increase in synchrony between peaks in PN and IN activity (in comparison with the case where NMDA receptors are absent – figure 3.3B, bottom panel). The decreased time or phase lag between peaks in PN and IN activity suggests a diminishing of the dependence of IN spike bursts on phasic PN input.

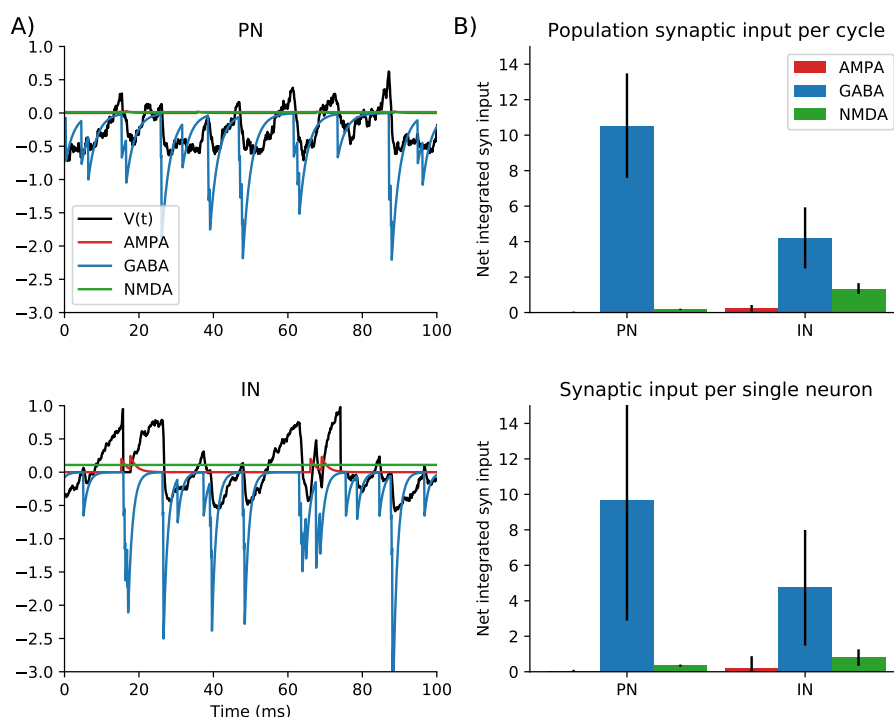


Figure 3.7. Model synaptic inputs with active NMDA receptors. A) Membrane potential, excitatory synaptic input through AMPA or NMDA receptors, and inhibitory GABAergic input to a single representative PN (top) or IN (bottom) in the network. B) Top: Net AMPA- or NMDA-mediated excitatory synaptic input or inhibitory (GABAergic) synaptic input to a PN or IN during an oscillation cycle; data are collected during a fixed oscillation cycle and averaged over all PNs or INs within the network. Bottom: Net AMPA- or NMDA-mediated excitatory synaptic input or inhibitory (GABAergic) synaptic input to a PN or IN during an oscillation cycle; data are collected for a single PN or IN and averaged over 67 oscillation cycles. Net input to a cell during a cycle is computed via numerical integration. Error bars represent standard deviation.

Figure 3.7A shows the membrane potential and AMPA-mediated excitatory, $GABA_A$ -mediated inhibitory, and NMDA-mediated input current for a sample PN (top) and IN (bottom) within the network; figure 3.7B (bottom) shows the excitatory (AMPA-mediated), inhibitory ($GABA_A$ -mediated) and NMDA input to a sample PN and IN in an oscillation cycle (averaged over multiple cycles), while figure 3.7B (top) shows the average excitatory, inhibitory, and NMDA input to all PNs and all INs in a sample oscillation cycle. Figure 3.7 shows that the NMDA current

impinging upon PNs and INs within the network is relatively small in magnitude, and we find that this is necessary to maintain network oscillations – further strengthening of the NMDA current tends to cause rampant firing and desynchronization. Due to the slower time course of NMDA receptors, NMDA input provides a relatively tonic, small excitatory input to neurons within the network (an input that oscillates less sharply with PN firing rate oscillations than AMPA-mediated input), and hence serves to increase the overall excitability of network cells; in particular, the excitability of INs, which receive relatively higher levels of NMDA input than PNs, rises disproportionately, which likely explains the reduction in firing rates seen after NMDA activation (compare figures 3.6A and 3.2B). Increased excitability implies that, following the initiation of an inhibitory barrage, a more rapid rise in IN spiking leads to a more rapid curtailment of IN activity via IN→IN synaptic inhibition, and this, along with the increase in excitation to PNs via active NMDA receptors, allows PNs to recover more quickly from IN inhibition. Furthermore, IN spike bursts are less dependent on phasic AMPA-mediated excitation from PNs, and therefore INs need not await significant AMPA-mediated input prior to spiking, yielding a smaller time lag between PN and IN spike bursts (compare figures 3.6D and 3.2C or figures 3.6E and 3.3B, bottom panel). Both of these phenomena likely contribute to the observed decrease in the oscillation period of the network.

Figure 3.6F shows the distribution of instantaneous LFP oscillation cycle frequencies in the presence and absence of NMDA receptors; without NMDA receptors, there is a narrow distribution of cycle frequencies with a peak at ~ 40 Hz, while the activation of NMDA receptors leads to a broader distribution with the peak occurring at a higher frequency of ~ 60 -70 Hz, similar to the cycle frequency distributions observed experimentally (Mann and Mody, 2010). In order to investigate the impact of NMDA-mediated currents, as well as AMPA- and GABA_A-mediated currents, on instantaneous cycle frequency, we measured the net amount of each current received by either all neurons within the network, all PNs within the network, or all INs within the network within individual oscillation cycles, and we examined the correlation of each measurement to instantaneous cycle frequency (figure 3.8). Figure 3.8C shows, expectedly, a strong inverse correlation between the level of GABA_A-mediated currents within a cycle and cycle frequency – the greater the amount inhibition generated by INs within a cycle, the greater the length of time required for PNs to recover and initiate a subsequent spike burst, lengthening the current cycle and prolonging the inception of the next cycle. Figure 3.8B shows that there is an inverse correlation, though a milder one, between the level of AMPA-mediated currents within a cycle and

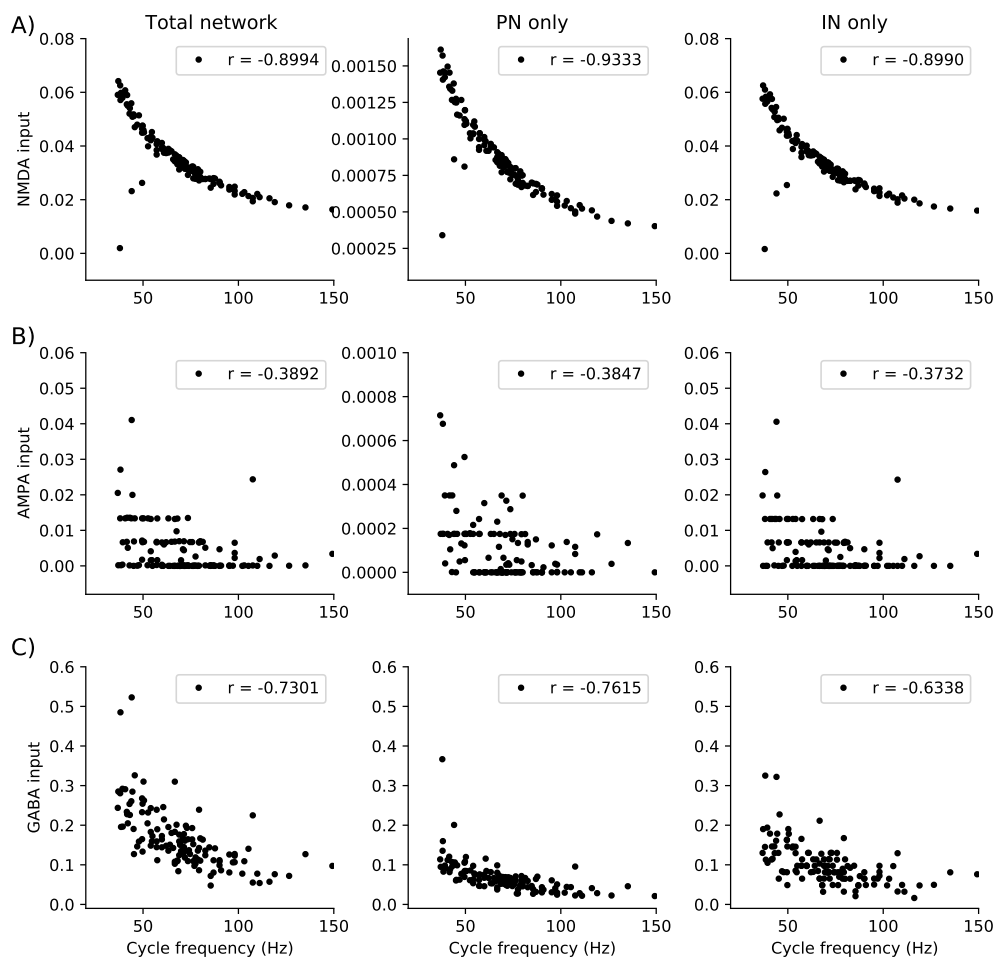


Figure 3.8. Scatterplots, in the model with active NMDA receptors, showing the relationship between instantaneous cycle frequency and average NMDA-mediated (A), AMPA-mediated (B), or GABA-mediated (C) input to all cells in the network (left column), all PNs in the network (middle column), or all INs in the network (right column) during a cycle. Average input of a particular type to a population during an oscillation cycle is computed via numerical integration of the current impinging upon a single cell during the cycle, averaged over all cells within the population. A total of 128 oscillation cycles are plotted in each panel.

cycle frequency as well; this is likely due to stronger phasic AMPA-mediated input from PNs causing a more robust burst of IN spikes, which in turn lengthens subsequent PN suppression and delays the onset of the next cycle.

Interestingly, figure 3.8A shows that there is a highly robust inverse correlation between the level of NMDA-mediated currents within a cycle and cycle frequency – thus, when NMDA receptors are active, cycles of higher frequency tend to have *lower* amounts of NMDA-mediated current seeping through the network, despite the fact that the cycle frequency distribution in

general is right-shifted (as well as broadened) in comparison to the case of absent NMDA receptors (figure 3.6F). The dynamics underlying this result are discussed in more detail within the next section (*Mechanism of Gamma Oscillations*); we first further parse network dynamics by separately examining the effects on the system when NMDA receptors are present only on INs or only on PNs. Placing NMDA receptors on INs alone tends to considerably increase cycle frequency to above 100 Hz (figure 3.9A,B, left panels), while when NMDA receptors are present only on PNs cycle frequency tends to decrease slightly to below 40 Hz (figure 3.9A,B, right panels); accordingly, instantaneous cycle frequency distributions show a broad distribution of cycle frequencies centered at ~ 100 Hz when NMDA receptors are present on INs alone and narrow distribution of cycle frequencies centered at ~ 35 Hz when NMDA receptors are present on PNs alone (figure 3.9C).

This suggests that NMDA receptors on INs versus PNs have opposing effects – NMDA receptors on INs tend to raise cycle frequency and increase variability in the oscillation period across cycles, while NMDA receptors on PNs tend to somewhat lower cycle frequency and lead to small variability in the oscillation period across cycles. The latter observation can be explained by the NMDA current, despite being small in amplitude (figure 3.7B), likely being capable of bolstering the firing rate of PNs during a spike burst initiated by external input, leading to a stronger subsequent IN spike burst and prolonged PN suppression prior to the beginning of the next cycle. The former observation arises from the relatively tonic NMDA current to INs being capable of inducing IN spiking without the need for significant AMPA-mediated input – INs both fire more rapidly in response to a PN spike burst as well as suppress each other more rapidly once they begin to spike, shortening the period of the oscillation cycle; moreover, without INs requiring significant PN input to spike, the orderly procession of PN spiking leading to IN spiking is less rigid than in the absence of NMDA receptors on INs, and there is greater variability in the timing of IN spike bursts (and hence a broader distribution of instantaneous cycle frequencies).

3.2.3 Mechanism of Gamma Oscillations

Two general mechanisms, the ‘I-I’ model and the ‘E-I’ model, for the emergence of gamma oscillations in networks of inhibitory and excitatory neurons have been proposed (for a review, see (Buzsaki, and Wang, 2012)). In the ‘I-I’ mechanism, the inhibitory neurons form an effectively independent subnetwork capable of generating gamma oscillations, with oscillations in the inhibitory subnetwork arising due to interconnections among the inhibitory cells – a burst of

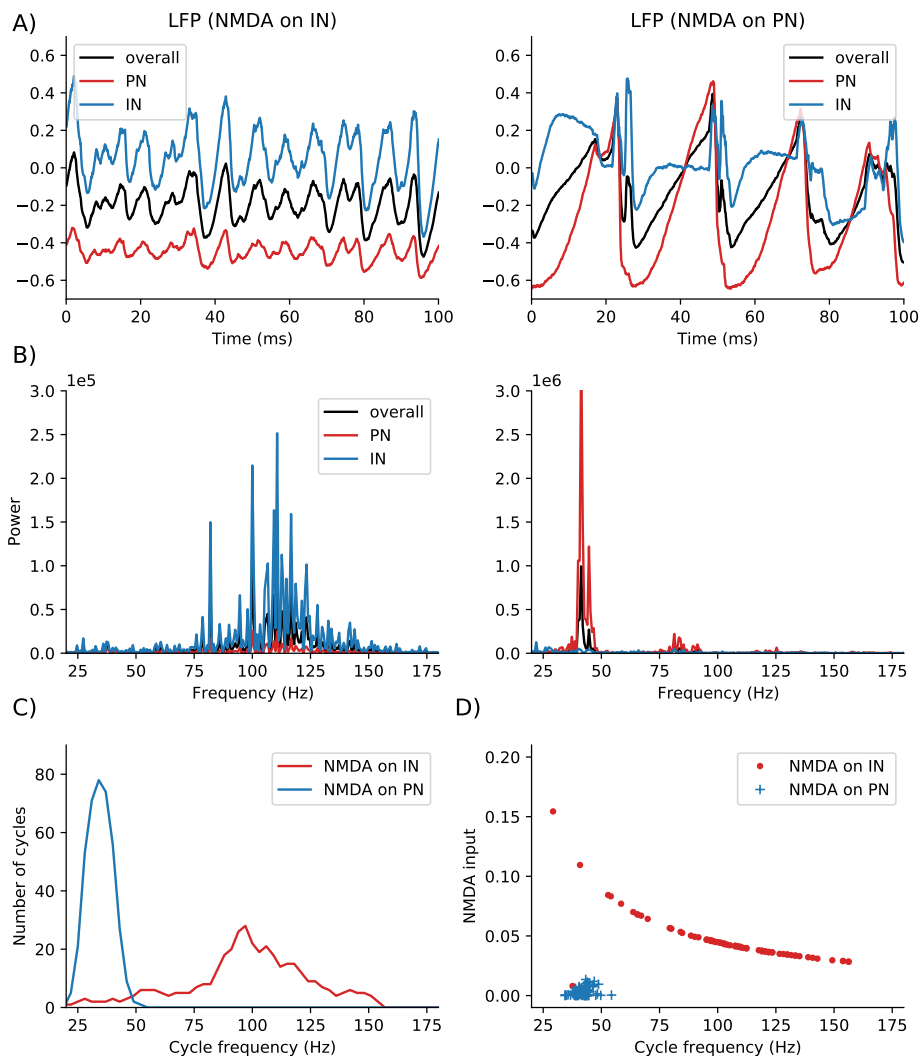


Figure 3.9. Model behavior with active NMDA receptors on either INs alone or PNs alone. Relative to baseline, parameters governing NMDA receptor dynamics are tuned in the case of NMDA receptors on INs alone and PNs alone in order to match model oscillatory behavior as closely as possible to that observed experimentally with NMDA receptor activation (see Methods for details). A) Local field potential by cell type, computed as the average membrane potential of all cells, all PNs, or all INs within the network, in the case of NMDA receptors on INs alone (left) or PNs alone (right). B) Power spectra of the local field potentials shown above in A). C) Distribution of instantaneous cycle frequency, in the two cases of NMDA receptors on INs alone or PNs alone. Data points represent number of cycles within 15 Hz bins, using a 1 Hz sliding window; a total of 80 cycles were collected for each of the two cases. D) Scatterplot, in the two cases of NMDA receptors on INs alone or PNs alone, showing the relationship between instantaneous cycle frequency and average NMDA-mediated input to all cells in the network during a cycle. NMDA-mediated input to a cell during an oscillation cycle is computed via numerical integration of the NMDA-mediated current impinging upon the cell during the cycle. A total of 80 oscillation cycles are plotted for each case.

spikes from inhibitory neurons results in silencing of the inhibitory subnetwork, and once the inhibition subsides another burst of inhibitory cell spikes ensues, beginning the cycle anew. In the pure 'I-I' mechanism, fast excitatory synapses play no role in the generation of gamma oscillations, and excitatory cell spikes simply occur during lulls in inhibition (Whittington, Traub, and Jefferys, 1995; Wang and Rinzel, 1992; Wang and Buzsaki, 1996; Traub et al., 1996). In the 'E-I' mechanism, oscillations occur as a consequence of phasic excitatory cell input to inhibitory cells – a burst of excitatory cell spikes results in a burst of inhibitory cell spikes, with inhibition then silencing both excitatory and inhibitory cells, and once the inhibition subsides another burst of excitatory cell spikes occurs that begins the next oscillation cycle. In the pure 'E-I' mechanism, the inhibitory cells are incapable of significant spiking on their own, and hence spike bursts of inhibitory cells are dependent on fast, phasic excitatory input from the excitatory cells (Fisahn et al., 1998; Mann et al., 2005; Wilson and Cowan, 1972; Leung, 1982; Ermentrout and Kopell, 1998; Borgers and Kopell, 2003; Brunel and Wang, 2003; Geisler, Brunel, and Wang, 2005).

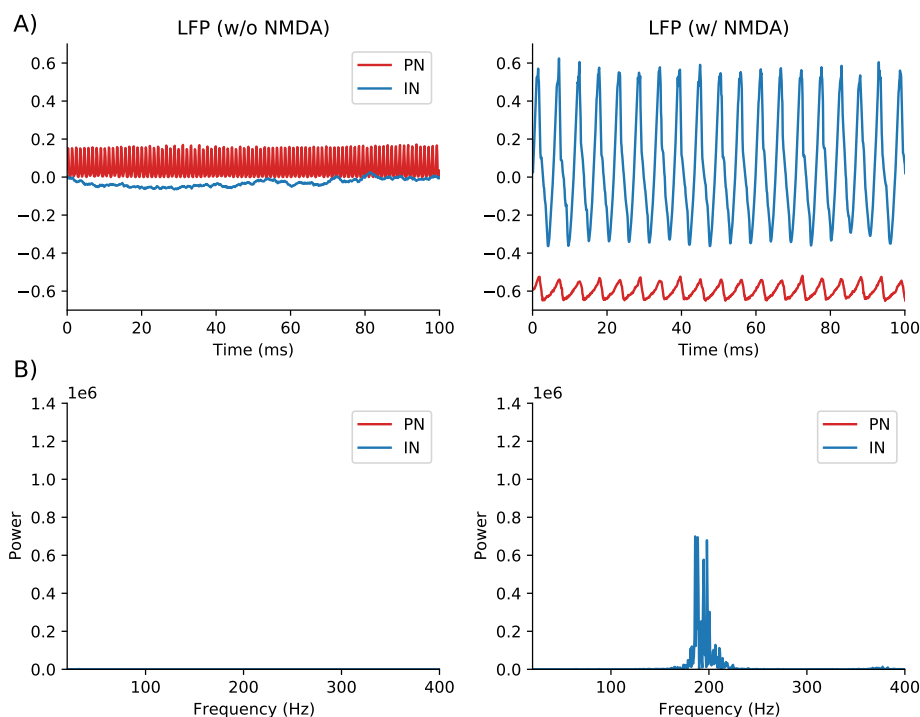


Figure 3.10. Oscillatory properties of the network following removal of AMPA receptors on INs alone, in the absence (left) or presence (right) of active NMDA receptors. A) Local field potential by cell type, computed as the average membrane potential of all PNs or all INs within the network. B) Power spectra of the LFPs shown above in A).

In the pure 'E-I' mechanism, since a PN spike burst is necessary to trigger an IN spike burst,

the associated conduction and synaptic delays lead to a substantial lag between PN and IN spikes (up to a 5 ms time lag or a $\frac{\pi}{2}$ phase lag (Leung, 1982), consistent with the time and phase lag observed in the absence of NMDA receptors in our model; see figures 3.2C and 3.3B). In the pure 'I-I' mechanism, the mean time lag between PN and IN spikes is likely to be closer to zero – since the 'I' subnetwork generates oscillations independently (without need of PN input), once the inhibition to 'E' and 'I' cells ensuing from an 'I' spike burst subsides, *both* 'E' and 'I' cells can produce a spike burst during the lull in inhibition, relatively independently of each other. In our model, the presence of NMDA receptors leads to a substantial diminishing of the time and phase lag between PN and IN spikes (figure 3.6D,E), indicating that the addition of NMDA receptors leads to a shift in the oscillation mechanism from the 'E-I' to the 'I-I' mechanism (indeed, the large standard deviation in the time lag between PN and IN peaks in figure 3.6D suggests that PN and IN spike bursts occur relatively independently of each other when NMDA receptors are active).

In order to further examine this, we selectively sever AMPA synapses from PNs to INs in our network, and in figure 3.10 we plot the separated PN and IN field potentials of the model, along with their associated power spectra, in the case that NMDA receptors are present (figure 3.10, right panels) or absent (figure 3.10, left panels) in this scenario. The left panels of figure 3.10 show that, without NMDA receptors, a lack of AMPA input to INs yields a relatively flat IN field potential (the external excitation to INs is insufficient to cause significant spiking), while PNs spike repeatedly at high rates (due to a lack of substantial inhibition from INs), and the network as a whole does not oscillate. This indicates that INs are incapable of substantial activity without AMPA input and (in the model with intact PN→IN AMPA synapses, but no NMDA synapses) gamma oscillations must arise due to phasic AMPA input from PNs to INs (i.e., through the 'E-I' mechanism). The right panels of figure 3.10 show that, with active NMDA receptors, the IN field potential exhibits oscillatory activity even without phasic PN→IN AMPA input, and that IN oscillations are capable of establishing a coherent, network-wide oscillatory state. It follows that in the full network (with PN→IN AMPA synapses and active NMDA) tonic NMDA input to INs is sufficient to allow the IN subnetwork to oscillate independently, though oscillations occur at a lower frequency than in the absence of PN→IN AMPA synapses (compare figures 3.10B,right and 3.6C), likely due (in the case of active PN→IN AMPA synapses) to PN spike bursts providing an impetus for larger IN spike bursts, prolonging the subsequent inhibitory lull and extending oscillation cycle length.

Thus, the presence or absence of NMDA receptors causes our full model to switch between two distinct dynamic regimes – in the absence of NMDA receptors, gamma oscillations occur via the pure ‘E-I’ mechanism, while active NMDA synapses lead to a shift towards the ‘I-I’ mechanism (with this shift due primarily to NMDA receptors on INs, as shown in figure 3.9 and discussed in the previous section). This explains several interesting results produced by our model. The cycle frequency distribution with active NMDA receptors (figure 3.6F) appears bimodal, with a smaller peak at ~ 40 Hz and a larger peak at ~ 60 -70 Hz. This bimodality can likely be attributed to varying levels of NMDA-mediated currents seeping through the network during different oscillation cycles – cycles with minimal NMDA currents operate within the ‘E-I’ regime (leading to a narrow distribution of frequencies for these cycles centered at ~ 40 Hz), while cycles with NMDA-induced current intensity surpassing a certain threshold level operate within the ‘I-I’ regime (leading to a broader distribution of frequencies for these cycles with a peak at ~ 60 -70 Hz).

This further provides an explanation for the rather counterintuitive result that, with NMDA synapses active, there tends to be a strong inverse correlation between the level of NMDA currents permeating the network during a cycle and instantaneous cycle frequency (figure 3.8A); this occurs because, in the presence of significant NMDA currents, the network is operating within a different regime than in the absence of such currents. When NMDA-mediated current levels surpass a certain threshold, the network operates within the ‘I-I’ regime, and *within this regime*, baseline oscillations tend to occur at within a high frequency range peaking at ~ 60 -70 Hz, with higher levels of NMDA leading to lower instantaneous cycle frequencies within the frequency range of the ‘I-I’ regime (likely due to a greater level of NMDA currents permeating the network during a cycle leading to an enhanced IN spike burst, a prolonged subsequent lull in activity induced by inhibition, and an extended cycle length). When NMDA currents are absent, the network operates within the ‘E-I’ regime, with a baseline oscillation frequency of ~ 40 Hz, and instantaneous cycle frequency is distributed within the frequency range of the ‘E-I’ regime. Indeed, figure 3.8A (as well as figure 3.9D in the subplot of NMDA receptors on INs only) show several outlying data points that appear to subvert the noticeably decreasing trend – these seemingly anomalous data points actually represent cycles in which the level of NMDA currents seeping through the network have fallen below the threshold required to sustain the ‘I-I’ regime, causing the network to briefly revert to the ‘E-I’ regime and hence oscillate within the ~ 40 Hz frequency range characteristic of this mechanism. Thus, we find that within the range

of NMDA current levels that are sufficiently strong to sustain an 'I-I' mechanism of gamma oscillations, oscillations occur within the higher frequency band characteristic of this regime and there is an inverse correlation between the level of NMDA currents permeating the network and instantaneous cycle frequency, while when NMDA current levels fall below the level required to sustain the 'I-I' mechanism of gamma oscillations, the network switches to the 'E-I' mechanism and oscillations occur within the 'E-I' regime's lower frequency band.

3.3 Discussion

In this work, we develop a model of the CA3 subfield of the hippocampus and examine the generation of carbachol-induced gamma oscillations in the presence and absence of NMDA receptors. We show that, in the absence of NMDA receptors, PN and IN firing rates in our model, the lag between PN and IN spike bursts, and excitatory and inhibitory synaptic dynamics match those observed experimentally (Hajos et al., 2004; Hajos and Paulsen, 2009; Oren et al., 2006; Zemankovics et al., 2013; Mann et al., 2005; Oren et al., 2006), and our model supports the hypothesis that ~ 40 Hz carbachol-induced gamma oscillations within CA3 are produced via the pure 'E-I' mechanism (Fisahn et al., 1998; Mann et al., 2005). In the presence of NMDA receptors, we show that our model exhibits a reduced time lag between PN and IN spike bursts, as well as an increase in gamma oscillation frequency and broadening of the cycle frequency distribution, as observed experimentally (Mann and Mody, 2010). We find that, in our model, NMDA receptors on INs specifically tend to increase the frequency of gamma oscillations, a prediction that can be experimentally tested. Remarkably, we find an *inverse* relationship between between the net NMDA current permeating the network during an oscillation cycle and cycle frequency, and we suggest that this can be explained by the network operating within distinct dynamic regimes in the case of no (or minimal) NMDA currents versus sufficiently strong NMDA currents. Accordingly, we show that the introduction of NMDA synapses into the system leads to a shift in the mechanism of gamma oscillations – without NMDA receptors, the model generates gamma oscillations via the pure 'E-I' mechanism, while with NMDA receptors, the 'I-I' mechanism tends to dominate in the generation of oscillations. Further experimental work will be required to test these predictions of our model.

3.3.1 Model Parameters

In our CA3 model, as observed empirically (Andersen et al., 2007), PNs outnumber INs, and synaptic connectivity within and between the PN and IN populations is sparse, in agreement with prior models (Traub et al., 1996; Wang and Buzsaki, 1996). The temporal dynamics and latencies associated with fast synapses (PN \rightarrow PN and PN \rightarrow IN AMPA synapses and IN \rightarrow IN and IN \rightarrow PN GABA_A synapses) have been well elucidated experimentally (Bartos et al., 2002), and the parameters governing these synapses in our model have been chosen to approximate experimental values. The temporal dynamics of NMDA receptor-mediated synaptic transmission within CA3, however, have not been elucidated experimentally, though studies indicate that differing subtypes of NMDA receptors are present on PNs versus INs (Brandalise et al., 2016; Berg et al., 2013; Nakazawa et al., 2002; Nakazawa et al., 2003; Mann and Mody, 2010), and hence it is possible that the temporal dynamics of NMDA receptors on PNs are different from those on INs. Due to a lack of available data on the dynamics of NMDA receptors within CA3, we set the temporal dynamics of NMDA receptors on PNs and INs in our model to be identical, and we adapted our NMDA dynamics from the classic NMDA model of (Moradi et al., 2013); further experimental work on NMDA dynamics within CA3 will allow more physiologically detailed modeling.

3.3.2 Other Models

While prior models have examined the emergence of gamma oscillations in excitatory and inhibitory networks, this is the first modeling study, to our knowledge, that has specifically investigated the effect of NMDA activation on carbachol-induced gamma oscillations within CA3. The two primary proposed models of gamma oscillation, discussed above, are the 'E-E' and 'I-I' mechanisms (Buzsaki, and Wang, 2012). The 'E-I' mechanism, due to the need for phasic excitation to trigger inhibitory spikes, necessarily implies a significant lag between excitatory and inhibitory spike bursts (Leung, 1982), which is a noted feature of gamma oscillations observed in experimental preparations (Mann et al., 2005; Hajos and Paulsen, 2009; Bragin et al., 1995; Csicsvari et al., 2003; Hasenstaub et al., 2005; Tiesinga and Sejnowski, 2009) and in our model without NMDA receptors. In the 'I-I' mechanism, a tonic excitatory drive to the inhibitory cells leads to homogeneous oscillations with little variation in cycle period (Kopell and Ermentrout,

2002), while a more stochastic excitatory drive to the inhibitory cells leads to a greater irregularity of cycle periods (Brunel and Wang, 2003; Geisler, Brunel, and Wang, 2005; Brunel and Hakim, 1999; Ardid et al., 2010; Economo and White, 2011). In our model, the NMDA drive to INs, though relatively tonic (compared to fast AMPA and GABA_A synapses within the model), exhibits some fluctuations over long time scales due to variations in PN firing rates, and hence leads to some variation in cycle periods (see the subplot of figure 3.9C in which NMDA receptors are present only on INs). In the presence of a fluctuating drive, network synchrony is expected to diminish (as seen in our model when NMDA receptors are active; compare figures 3.6C and 3.3A, bottom panel), though studies show that gap junction coupling among 'I' cells can serve to enhance network synchrony (Traub et al., 2001; Gibson, Beierlein, and Connors, 1999; Buhl et al., 2003). In our model, we do not incorporate gap junction coupling among INs, though it is possible that, within the CA3 subfield, gap junction coupling among INs exists and may serve to promote stronger network synchrony in the presence of significant NMDA activation.

3.4 Methods

We construct a model of hippocampal gamma oscillations in the CA3 region of the hippocampus as a network of 200 excitatory pyramidal neurons (PNs) and 50 inhibitory interneurons (INs) (Witter, 2007; Bartos, Alle, and Vida, 2011; Andersen et al., 2007), which is used to simulate experimental conditions from an in vitro study (Mann and Mody, 2010) that knocks out specific subunits on δ -GABA_A receptors that usually prevent NMDA activation, such that NMDA currents are able to be exogenously controlled by cholinergic agonists. PNs and INs form random synapses with each other, as determined by parameters governing connectivity for each combination of pre- and postsynaptic cell types; all PN outputs synapse onto AMPA and NMDA receptors, while IN outputs synapse onto GABA_A-type receptors (Bartos, Alle, and Vida, 2011; Mann and Paulsen, 2007; Lawrence and McBain, 2003; Bartos et al., 2002). To model the control condition, we implement only AMPA and GABA currents in the model, which are postsynaptic to PNs and INs respectively. We simulate the experimental activation of NMDA receptors by introducing a current specific to NMDA into the model, which is postsynaptic to only PNs.

3.4.1 Model Equations

We construct a conductance based model consisting of 200 excitatory PNs and 50 inhibitory INs. The membrane potential of neuron k, j is governed by a reduced dimensional integrate-and-fire model of a cortical cell:

$$\begin{aligned} \dot{V}^{k,j} = & -g_L(V^{k,j}(t) - E_{\text{rest}}) - g_{\text{AMPA}}^{k,j}(V^{k,j}(t) - E_{\text{AMPA}}) \\ & - g_{\text{GABA}}^{k,j}(V^{k,j}(t) - E_{\text{GABA}}) + I_{\text{NMDA}}^{k,j}(t) + \zeta^{k,j}(t), \end{aligned} \quad (3.1)$$

where $k \in \{\text{PN}, \text{IN}\}$, while $j \in \{1, 2, \dots, 200\}$ for $k = \text{PN}$ and $j \in \{1, 2, \dots, 50\}$ for $k = \text{IN}$. $V^{k,j}$ is the non-dimensional membrane potential, g_L (in ms^{-1}) is the leak conductance, g_α is conductance for current type $\alpha \in \{\text{AMPA}, \text{GABA}\}$, E_α is reversal potential, $\zeta^{k,j}$ denotes external input that provides excitation to the network, and $I_{\text{NMDA}}^{k,j}(t)$ is the synaptic NMDA current (in ms^{-1}), which is set to 0 in the baseline model without NMDA activation. $E_{\text{rest}} = 0$ is the resting potential, and a spike is recorded when $V^{k,j} \rightarrow 1^-$, at which point $V^{k,j}$ is instantaneously reset to E_{rest} . A refractory period is simulated by holding $V^{k,j}$ at E_{rest} for 2 ms following a spike. Details of the reduced dimensional model are given in (Tao et al., 2004).

AMPA and GABA currents: A spike of a neuron presynaptic to neuron k, j leads to a jump in $g^{k,j}(t)$ followed by exponential decay, after a manually imposed synaptic latency. Let $n^{k,j}$ denote the total number of presynaptic spikes that impinged upon neuron k, j during a trial. If the r^{th} presynaptic spike occurs at time $t_r^{k,j}$, and $m \in \{\text{PN}, \text{IN}\}$ is the type of the presynaptic neuron, the conductance $g^{k,j}(t)$ induced in neuron k, j at time t is given by the following:

$$i_r^{k,j}(t) = \begin{cases} 0 & t < t_r^{k,j} + l_m^k, \\ A_m^k e^{-\frac{t - (t_r^{k,j} + l_m^k)}{\tau_m^k}} & \geq t_r^{k,j} + l_m^k. \end{cases} \quad (3.2)$$

$$g^{k,j}(t) = \sum_{r=1}^{n^{k,j}} i_r^{k,j}(t). \quad (3.3)$$

l_m^k denotes the latency (synaptic delay), τ_m^k dictates the decay rate, and A_m^k indicates the amplitude of an input from a neuron of type $m \in \{\text{PN}, \text{IN}\}$ to a neuron of type $k \in \{\text{PN}, \text{IN}\}$.

NMDA currents: NMDA receptors have an unique activation mechanism modeled here as an activation and deactivation term, adapted from the model by (Moradi et al., 2013). $I_{\text{NMDA}}(t)$

is set to 0 in models of the control case (absence of NMDA activation), and in models of the test condition (where NMDA receptors are active), a spike of a PN presynaptic to neuron k, j leads to a jump in $I_{\text{NMDA}}^{k,j}(t)$ followed by exponential decay, after a manually imposed synaptic latency. The NMDA current $I_{\text{NMDA}}^{k,j}(t)$ to neuron k, j in the network is governed by the following equations:

$$I_{\text{NMDA}}^{k,j} = \frac{-B^{k,j} - A^{k,j}}{8 + e^{-8(V^{k,j} - 0.6)}} (V^{k,j} - E_{\text{NMDA}}), \quad (3.4)$$

$$\dot{A}^{k,j} = -\frac{A^{k,j}}{\tau_A}, \quad (3.5)$$

$$\dot{B}^{k,j} = -\frac{B^{k,j}}{\tau_B}, \quad (3.6)$$

where $A^{k,j}$ denotes a fast time scale activation and $B^{k,j}$ denotes a slow time scale deactivation. A presynaptic PN spike at time t^* is modeled by an instantaneous upward jump in $A^{k,j}$ and $B^{k,j}$ at time t^* . Parameter values governing NMDA dynamics are given in table 2. Since the deactivation term is significantly slower than the activation term, lingering NMDA currents provide tonic excitation to the system (Banke and Traynelis, 2003).

3.4.2 Parameters

probability	amplitude (A) (ms^{-1})	latency (l) (ms)	decay (τ) (ms)
$P_{\text{PN}}^{\text{PN}} = 0.3$	$A_{\text{PN}}^{\text{PN}} = 0.02$	$l_{\text{PN}}^{\text{PN}} = 1.0$	$\tau_{\text{PN}}^{\text{PN}} = 1.7$
$P_{\text{IN}}^{\text{PN}} = 0.3$	$A_{\text{IN}}^{\text{PN}} = 0.2$	$l_{\text{IN}}^{\text{PN}} = 2.3$	$\tau_{\text{IN}}^{\text{PN}} = 1.6$
$P_{\text{PN}}^{\text{IN}} = 0.45$	$A_{\text{PN}}^{\text{IN}} = 0.65$	$l_{\text{PN}}^{\text{IN}} = 0.6$	$\tau_{\text{PN}}^{\text{IN}} = 2.3$
$P_{\text{IN}}^{\text{IN}} = 0.45$	$A_{\text{IN}}^{\text{IN}} = 0.65$	$l_{\text{IN}}^{\text{IN}} = 1.1$	$\tau_{\text{IN}}^{\text{IN}} = 1.2$
$P_{\text{PN}}^{\text{PN}} = 0.3$	*	$l_{\text{PN}}^{\text{PN}} = 1.0$	*
$P_{\text{IN}}^{\text{PN}} = 0.3$	*	$l_{\text{IN}}^{\text{PN}} = 2.3$	*

Table 1. Parameter values for the model. See Table 2 for detailed NMDA terms.

In addition, $E_{\text{AMPA}} = E_{\text{NMDA}} = 4.67$, $E_{\text{GABA}} = -0.67$, $g_L = 0.05ms^{-1}$; the external excitation $\zeta^{k,j}$ is modeled as white noise with mean and standard deviation given by 0.08 ± 0.4 for $k = \text{PN}$ and 0 ± 0.2 for $k = \text{IN}$. Synaptic densities are kept within a reasonable range of

the convergence/divergence factor described in (Wang and Buzsaki, 1996), wherein a scaling factor M_{syn} is developed from experimental network connectivity estimates to fit networks of n neurons, with outgoing synaptic density set higher for INs than PNs. NMDA receptors are empirically found to be present on both PNs (Brandalise et al., 2016; Berg et al., 2013; Nakazawa et al., 2002; Nakazawa et al., 2003) and INs (Mann and Mody, 2010); accordingly, we simulate the introduction of NMDA receptor activation on both cell types. In addition, we examine the effect of activating NMDA receptors on individual subpopulations of neurons to isolate the dynamical effects of NMDA currents on PNs versus INs, in which case parameter values are adjusted to ensure physiologically reasonable dynamics. We also simulate pharmacological experiments blocking either AMPA or GABA currents by setting the amplitude of the current being removed to 0. Parameters for synaptic amplitudes, latencies, and decay rates are adapted from and kept within a close range of empirically derived values (Bartos et al., 2002). NMDA currents have slower decay time scales than AMPA and GABA, and thus NMDA generated excitation lasts longer, and has a unique activation mechanism (Banke and Traynelis, 2003), with governing parameter values shown in table 2.

Latency parameters were chosen to be both consistent with empirical latency estimates and to match the experimental observation of a delay of a few ms between PN and IN peaks during network activity in the absence of NMDA activation (Hajos and Paulsen, 2009; Buzsaki, and Wang, 2012). Decay rates for the NMDA activation and deactivation terms are given by $\tau_A = 3.5$ ms and $\tau_B = 436.9$ ms.

	IN (NMDA to both)	PN (NMDA to both)	IN (NMDA to IN)	PN (NMDA to PN)
ΔA (ms^{-1})	.0008	.00002	.002	.0000009
ΔB (ms^{-1})	.0012	.00004	.003	.0000006

Table 2. Jump in the activation and deactivation variables A and B in the NMDA equations caused by a presynaptic PN spike. Values shown are for postsynaptic INs and PNs, in the cases where NMDA receptors are present on both cell types, on INs only, or on PNs only.

3.4.3 Data Analysis

Firing rates are plotted as histograms of spike counts, with a bin size of 5 ms and a sliding window of 1 ms, and are smoothed using convolution by a Gaussian kernel, using Python's SciPy library. Local field potentials (LFPs) are calculated as the average V_m for all cells at a

given time step. Times of peak spiking for PNs and INs are found using SciPy's peak detection algorithm. A single oscillation cycle begins at a peak in the LFP and ends at the next peak; to quantify phase differences, this range of values is mapped to a $(-\pi, \pi)$ range. Histograms of peak phase have bin sizes of $\frac{\pi}{4}$ and windows of $\frac{\pi}{100}$ (figures 3 and 6).

Distributions of instantaneous cycle frequency are plotted in 15 Hz bins with a 1 Hz sliding window. Synaptic inputs are computed via numerical integration of the area between the curve of the current and 0 for either the entire time frame (for bar plots in figures 4 and 7) or for a single oscillation cycle (for scatterplots in figures 8 and 9). All power spectra are computed via fast Fourier transforms using SciPy, and their peaks are found via SciPy's peak detection algorithm.

Means, standard deviations, and correlations are calculated using Python's statistics library. Simulations are carried out using Euler's method with a time step of 0.01 ms and trial lengths of 2000 ms. Model code is freely available at <https://github.com/lma000/CA3OscModel>.

Chapter 4

Discussion

In these studies, we construct models of two cortical neural circuits that capture a range of experimentally generated results, as well as offer testable predictions. Studying systems neuroscience through simulation and modeling offers a unique way to analyze and deconstruct neural circuits through mechanistic constructions. By simulating empirical results, we can study emergent results arising from mechanisms and connections that we explicitly define, simultaneously allowing us to design a functional model of a particular system as well as make deductions about why those connections yield these results.

The first of these studies examines the generation of spike patterns from multiwhisker inputs to the rat barrel cortex using a network model built with LIF neuron models. In particular, we evaluate different and experimentally conflicting hypotheses of the mechanisms behind multiwhisker receptive fields. By simulating a number of experimental conditions from the literature, we show that lateral synaptic connections between layer IV somatosensory neurons between barrels can replicate a broad range of physiologically accurate behaviors, notably including results that the main competing hypothesis, feedforward connections, cannot easily capture (see figure 2.8). Namely, we simulate experiments severing GABA synapses and paired whisker deflections, as well as a number of comparing direction selectivity between PW and AW deflections. In particular, although information on lateral connections that can be used to generate empirical parameters is scant, we reproduce a number of figures from experimental papers with fairly high accuracy using our model. In fact, fitting parameters to a fairly narrow scope of empirical results allows us to extrapolate the range they can take and how the network would behave within these ranges (see figure 2.6), hinting at how these as of yet uncharacterized connections would work if this hypothesis is empirically true.

In the second study we evaluate mechanisms governing hippocampal gamma oscillations by

comparing the absence and activation of NMDA receptors PNs and INs in the CA3 subfield of the hippocampus. We model baseline 40 Hz oscillations in the control case, then examine the effect of simulating the activation of NMDA receptors first on all neurons in the network, and then individually on PNs or INs. Our results suggest that this causes a shift between the two regimes, 'E-I' and 'I-I', that are experimentally observed to generate gamma oscillations, and NMDA activity above a threshold level is what triggers this shift. Activation of NMDA in our model generally yields higher oscillation frequency, decreased phase difference between cycle peaks, and an increased range in cycle frequency distributions, in accordance with experimental results. In addition, within our model, activation of NMDA receptors on INs alone in general increases oscillation frequency, while NMDA receptors on PNs alone has little significant effect, an experimentally testable hypothesis that could support the hypothesis we model.

Both of these model specific mechanisms that previous work in the field does not; in the first study, the combination of modeling multiwhisker RFs and lateral connections has not yet been done, likely due to the scarcity of experimental data on such connections. Thus this study is one of the few that tries to study how they would work by fitting them to replicate empirical results. In the second, these particular results about NMDA activation on carbachol induced gamma oscillations have not yet been modeled, providing a different take on the classic models of the 'E-I' and 'I-I' gamma oscillation regimes, as well as positing a trigger that causes the shift between them. By explicitly setting connections in these models, we can draw more definitive cause-and-effect conclusions when we modify these connections between simulation conditions and observe emergent results. This offers us insight into the architecture and mechanisms behind these networks that would be difficult to conclude experimentally.

Acknowledgments

My heartfelt gratitude to Dr. Mainak Patel for all the time and effort he put into guiding me not only through these projects, but also through navigating research and academia as a whole. I would also like to thank Dr. Leah Shaw and Dr. Margaret Saha for serving on my committee, and for their much-appreciated encouragement and feedback.

Bibliography

- Agmon, A. et al. (1995). "Topological precision in the thalamic projection to neonatal mouse barrel cortex". In: *J Neurosci* 15(1 Pt 2), pp. 549–561.
- Andermann, M. and C. Moore (2006). "A somatotopic map of vibrissa motion direction within a barrel column". In: *Nat Neurosci* 9, pp. 543–551.
- Andersen, P. et al. (2007). "The hippocampus book". In: *Oxford University Press: New York, New York*.
- Ardid, S. et al. (2010). "Reconciling coherent oscillation with modulation of irregular spiking activity in selective attention: gamma-range synchronization between sensory and executive cortical areas". In: *J Neuroscience* 30, pp. 2856–2870.
- Armstrong-James, M., K. Fox, and A. Das-Gupta (1992). "Flow of excitation within rat barrel cortex on striking a single vibrissa". In: *J Neurophysiol* 68, pp. 1345–1358.
- Arnold, P., C. Li, and R. Waters (2001). "Thalamocortical arbors extend beyond single cortical barrels: an in vivo intracellular tracing study in rat". In: *Exp Brain Res* 136, pp. 152–168.
- Axmacher, N. et al. (2006). "Memory formation by neuronal synchronization". In: *Brain Res Rev.* 52, pp. 170–182.
- Banke, T. and S. Traynelis (2003). "Activation of NR1/NR2B NMDA receptors". In: *Nature Neurosci.* 6, pp. 144–152.
- Bartos, M., H. Alle, and I. Vida (2011). "Role of microcircuit structure and input integration in hippocampal interneuron recruitment and plasticity". In: *Neuropharmacology* 60, pp. 730–739.
- Bartos, M. et al. (2002). "Fast synaptic inhibition promotes synchronized gamma oscillations in hippocampal interneuron networks". In: *Proc Natl Acad Sci USA.* 99, pp. 13222–13227.
- Beaulieu, C. (1993). "Numerical data on neocortical neurons in adult rat, with special reference to the GABA population". In: *Brain Res* 609, pp. 284–292.
- Benowitz, L.I. and H.J. Karten (2004). "Organization of the tectofugal visual pathway in the pigeon: a retrograde transport study". In: *J Comp Neurol* 167.4, pp. 503–520.

- Berg, L. et al. (2013). "Pre- and postsynaptic localization of NMDA receptor subunits at hippocampal mossy fibre synapses". In: *Neuroscience* 230, pp. 139–150.
- Bernardo, K. and T. Woolsey (1987). "Axonal trajectories between mouse somatosensory thalamus and cortex". In: *J Comp Neurol* 258, pp. 542–564.
- Blitz, D.M. and W.G. Regehr (2005). "Timing and specificity of feed-forward inhibition within the LGN". In: *Neuron* 45, pp. 917–928.
- Borgers, C. and N. Kopell (2003). "Synchronization in networks of excitatory and inhibitory neurons with sparse, random connectivity". In: *Neural Comput* 15, pp. 509–538.
- Bragin, A. et al. (1995). "Gamma (40–100 Hz) oscillation in the hippocampus of the behaving rat". In: *J Neuroscience* 15, pp. 47–60.
- Brandalise, F. et al. (2016). "Dendritic NMDA spikes are necessary for timing-dependent associative LTP in CA3 pyramidal cells". In: *Nat Comm.* 7, p. 13480.
- Brecht, M. and B. Sakmann (2002a). "Dynamic representation of whisker deflection by synaptic potentials in spiny stellate and pyramidal cells in the barrels and septa of layer 4 rat somatosensory cortex". In: *J Physiol* 543(Pt 1), pp. 49–70.
- (2002b). "Whisker maps of neuronal subclasses of the rat ventral posterior medial thalamus, identified by whole-cell voltage recording and morphological reconstruction". In: *J Physiol* 538(Pt 2), pp. 495–515.
- Brumberg, J., D. Pinto, and D. Simons (1996). "Spatial gradients and inhibitory summation in the rat whisker barrel system". In: *J Neurophysiol* 76, pp. 130–140.
- Brunel, N. and V. Hakim (1999). "Fast global oscillations in networks of integrate-and-fire neurons with low firing rates". In: *Neural Comput* 11, pp. 1621–1671.
- Brunel, N. and X. Wang (2003). "What determines the frequency of fast network oscillations with irregular neural discharges? I Synaptic dynamics and excitation-inhibition balance". In: *J Neurophysiology* 90, pp. 415–430.
- Bruno, R. (2011). "Synchrony in sensation". In: *Current Opinion in Neurobiol* 21.5, pp. 701–708.
- Bruno, R. and B. Sakmann (2006). "Cortex is driven by weak but synchronously active thalamocortical synapses". In: *Science* 312.5780, pp. 1622–1627.
- Bruno, R. and D. Simons (2002). "Feedforward Mechanisms of Excitatory and Inhibitory Cortical Receptive Fields". In: *J Neurosci* 22, pp. 10966–10975.
- Bruno, R. et al. (2003). "Thalamocortical angular tuning domains within individual barrels of rat somatosensory cortex". In: *J Neurosci* 23, pp. 9565–9574.

- Buhl, D. et al. (2003). "Selective impairment of hippocampal gamma oscillations in connexin-36 knock-out mouse in vivo". In: *J Neuroscience* 23, pp. 1013–1018.
- Buzsaki, G., and XJ. Wang (2012). "Mechanisms of Gamma Oscillations". In: *Annu Rev Neurosci.* 35, pp. 203–225.
- Buzsaki, G. and A. Draguhn (2004). "Neuronal oscillations in cortical networks". In: *Science* 304, pp. 1926–1929.
- Campagner, D. et al. (2018). "What the whiskers tell the brain". In: *Neurosci* 368, pp. 95–108.
- Colgin, LL. (2011). "Oscillations and hippocampal-prefrontal synchrony". In: *Curr Opin Neurobiol.* 21, pp. 467–474.
- Colgin, LL. and EI. Moser (2010). "Gamma oscillations in the hippocampus". In: *Physiology (Bethesda)* 25, pp. 319–329.
- Courtemanche, R., JC. Robinson, and DI. Aponte (2013). "Linking oscillations in cerebellar circuits". In: *Front Neural Circuits* 7, p. 125.
- Cruikshank, S., T. Lewis, and B. Connors (2007). "Synaptic basis for intense thalamocortical activation of feedforward inhibitory cells in neocortex". In: *Nat Neurosci* 10, pp. 462–468.
- Csicsvari, J. et al. (2003). "Mechanisms of gamma oscillations in the hippocampus of the behaving rat". In: *Neuron* 37, pp. 311–322.
- Deng, C. and L.J. Rogers (1998). "Organisation of the tectorotundal and SP/IPS-rotundal projections in the chick". In: *J Comp Neurol* 394.2, pp. 171–185.
- Draguhn, A., M. Keller, and S. Reichinnek (2014). "Coordinated network activity in the hippocampus". In: *Front Neurol Neurosci.* 34, pp. 26–35.
- Economo, M. and J. White (2011). "Membrane properties and the balance between excitation and inhibition control gamma-frequency oscillations arising from feedback inhibition". In: *PLoS Comp Biol* 8, e1002354.
- Ermentrout, G. and N. Kopell (1998). "Fine structure of neural spiking and synchronization in the presence of conduction delays". In: *Proc Natl Acad Sci USA* 95, pp. 1259–1264.
- Fisahn, A. et al. (1998). "Cholinergic induction of network oscillations at 40 Hz in the hippocampus in vitro". In: *Nature* 394, pp. 186–189.
- Fox, K. (1994). "The cortical component of experience-dependent synaptic plasticity in the rat barrel cortex". In: *J Neurosci* 14, pp. 7665–7679.
- (2018). "Deconstructing the cortical column in the barrel cortex". In: *Neuroscience* 368, pp. 17–28.

- Fox, K. et al. (2003). "The origin of cortical surround receptive fields studied in the barrel cortex". In: *J Neurosci* 23, pp. 8380–8391.
- Fricker, D. and R. Miles (2000). "EPSP amplification and the precision of spike timing in hippocampal neurons". In: *Neuron* 28, pp. 559–569.
- Furuta, T., M. Deschenes, and T. Kaneko (2011). "Anisotropic distribution of thalamocortical boutons in barrels". In: *J Neurosci* 31, pp. 6432–6439.
- Gabernet, L. et al. (2005). "Somatosensory Integration Controlled by Dynamic Thalamocortical Feed-Forward Inhibition". In: *Neuron* 48.2, pp. 315–327.
- Geisler, C., N. Brunel, and X. Wang (2005). "Contributions of intrinsic membrane dynamics to fast network oscillations with irregular neuronal discharges". In: *J Neurophysiology* 94, pp. 4344–4361.
- Ghazanfar, A. and M. Nicolelis (1997). "Nonlinear processing of tactile information in the thalamocortical loop". In: *J Neurophysiol* 78, pp. 506–510.
- Gibson, J., M. Beierlein, and B. Connors (1999). "Two networks of electrically coupled inhibitory neurons in neocortex". In: *Nature* 402, pp. 75–79.
- Goldreich, D., H. Kyriazi, and D. Simons (1999). "Functional independence of layer IV barrels in rodent somatosensory cortex". In: *J Neurophysiol* 82, pp. 1311–1316.
- Gottlieb, J. and A. Keller (1997). "Intrinsic circuitry and physiological properties of pyramidal neurons in rat barrel cortex". In: *Exp Brain Res* 115, pp. 47–60.
- Gregoriou, GG., S. Paneri, and P. Sapountzis (2015). "Oscillatory synchrony as a mechanism of attentional processing". In: *Brain Research* 1626, pp. 165–182.
- Gulyas, AI. et al. (1993). "Hippocampal pyramidal cells excite inhibitory neurons through a single release site". In: *Nature* 366, pp. 683–687.
- Hajos, N. and O. Paulsen (2009). "Network mechanisms of gamma oscillations in the CA3 region of the hippocampus". In: *Neural Networks* 22, pp. 1113–1119.
- Hajos, N. et al. (2004). "Spike timing of distinct types of GABAergic interneuron during hippocampal gamma oscillations in vitro". In: *J Neurosci*. 24, pp. 9127–9137.
- Hanslmayr, S., BP. Staresina, and H. Bowman (2016). "Oscillations and Episodic Memory: Addressing the Synchronization/Desynchronization Conundrum". In: *Trends Neurosci*. 39, pp. 16–25.
- Harris, AZ. and JA. Gordon (2015). "Long-range neural synchrony in behavior". In: *Annu Rev Neurosci*. 38, pp. 171–194.

- Harris, R. and T. Woolsey (1983). "Computer-assisted analyses of barrel neuron axons and their putative synaptic contacts". In: *J Comp Neurol* 220, pp. 63–79.
- Hasenstaub, A. et al. (2005). "Inhibitory postsynaptic potentials carry synchronized frequency information in active cortical networks". In: *Neuron* 47, pp. 423–435.
- Hemelt, M. et al. (2010). "Consistency of angular tuning in the rat vibrissa system". In: *J Neurophysiol* 104, pp. 3105–3112.
- Higley, M. and D. Contreras (2007). "Frequency adaptation modulates spatial integration of sensory responses in the rat whisker system". In: *J Neurophysiol* 97, pp. 3819–3824.
- Jensen, K. and H. Killackey (1987). "Terminal arbors of axons projecting to the somatosensory cortex of the adult rat. I. The normal morphology of specific thalamocortical afferents". In: *J Neurosci* 7, pp. 3529–3543.
- Jortner, R.A., S.S. Farivar, and G. Laurent (2007). "A simple connectivity scheme for sparse coding in an olfactory system". In: *J Neurosci* 27, pp. 1659–1669.
- Joshi, B. and M. Patel (2013). "Encoding with synchrony: phase-delayed inhibition allows for reliable and specific stimulus detection". In: *J Theoretical Biol* 328, pp. 26–32.
- Katz, Y., J. Heiss, and I. Lampl (2006). "Cross-whisker adaptation of neurons in the rat barrel cortex". In: *J Neurosci* 26, pp. 13363–13372.
- Kawaguchi, Y. and Y. Kubota (1993). "Correlation of physiological subgroupings of nonpyramidal cells with parvalbumin- and calbindinD28k-immunoreactive neurons in layer V of rat frontal cortex". In: *J Neurophysiol* 70, pp. 387–396.
- Keller, A. and G. Carlson (1999). "Neonatal whisker clipping alters intracortical, but not thalamocortical projections, in rat barrel cortex". In: *J Comp Neurol* 412, pp. 93–94.
- Kida, H., S. Shimegi, and H. Sato (2005). "Similarity of direction tuning among responses to stimulation of different whiskers in neurons of rat barrel cortex". In: *J Neurophysiol* 94, pp. 2004–2018.
- Kopell, N. and G. Ermentrout (2002). "Mechanisms of phase-locking and frequency control in pairs of coupled neural oscillators". In: *Handbook on Dynamical Systems* New York: Elsevier, pp. 3–54.
- Kremer, Y. et al. (2011). "Late emergence of the vibrissa direction selectivity map in the rat barrel cortex". In: *J Neurosci* 31, pp. 10689–10700.
- Kwegyir-Afful, E. et al. (2005). "The Role of Thalamic Inputs in Surround Receptive Fields of Barrel Neurons". In: *J Neurosci* 25, pp. 5926–5934.

- Kyriazi, H. and D. Simons (1993). "Thalamocortical response transformations in simulated whisker barrels". In: *J Neurosci* 13, pp. 1601–1615.
- Kyriazi, H. et al. (1996). "Quantitative effects of GABA and bicuculline methiodide on receptive field properties of neurons in real and simulated whisker barrels". In: *J Neurophysiol* 75, pp. 547–560.
- Land, P., S. Buffer, and J. Yaskosky (1995). "Barreloids in adult rat thalamus: three dimensional architecture and relationship to somatosensory cortical barrels." In: *J Comp Neurol* 355, pp. 573–588.
- Lawrence, JJ. and CJ. McBain (2003). "Interneuron diversity series: containing the detonation-feedforward inhibition in the CA3 hippocampus". In: *Trends Neurosci.* 26, pp. 631–640.
- Le Cam, J. et al. (2011). "Spatial structure of multiwhisker receptive fields in the barrel cortex is stimulus dependent". In: *J Neurophysiol* 106, pp. 986–998.
- Lee, S., M. Friedberg, and F. Ebner (1994). "The role of GABA-mediated inhibition in the rat ventral posterior medial thalamus. I. Assessment of receptive field changes following thalamic reticular nucleus lesions". In: *J Neurophysiol* 71, pp. 1702–1715.
- Lee, S. and D. Simons (2004). "Angular tuning and velocity sensitivity in different neuron classes within layer 4 of rat barrel cortex". In: *J Neurophysiol* 91, pp. 223–229.
- Leitch, B., G. Laurent, et al. (1996). "GABAergic synapses in the antennal lobe and mushroom body of the locust olfactory system". In: *J Comp Neurol* 372, pp. 487–514.
- Leung, L. (1982). "Nonlinear feedback model of neuronal populations in hippocampal CA1 region". In: *J Neurophysiology* 47, pp. 845–868.
- Lisman, JE. and O. Jensen (2013). "The theta-gamma neural code". In: *Neuron* 77, pp. 1002–1016.
- Liu, R., M. Patel, and B. Joshi (2014). "Encoding whisker deflection velocity within the rodent barrel cortex using phase-delayed inhibition". In: *J Comput Neurosci* 37, pp. 387–401.
- Lubke, J. et al. (2000). "Columnar organization of dendrites and axons of single and synaptically coupled excitatory spiny neurons in layer 4 of the rat barrel cortex". In: *J Neurosci* 20, pp. 5300–5311.
- Mann, E. and I. Mody (2010). "Control of hippocampal gamma oscillation frequency by tonic inhibition and excitation of interneurons". In: *Nature Neurosci.* 13, pp. 205–212.
- Mann, E. and O. Paulsen (2007). "Role of GABAergic inhibition in hippocampal network oscillations". In: *Trends in Neurosci.* 30, pp. 343–349.

- Mann, EO. et al. (2005). "Perisomatic feedback inhibition underlies cholinergically induced fast network oscillations in the rat hippocampus in vitro". In: *Neuron* 45, pp. 105–117.
- Mittmann, W., U. Koch, and M. Häusser (2005). "Feed-forward inhibition shapes the spike output of cerebellar Purkinje cells". In: *J Physiol* 563, pp. 369–378.
- Moradi, K. et al. (2013). "A fast model of voltage-dependent NMDA receptors". In: *J Computational Neuroscience* 34, pp. 521–531.
- Nakazawa, K. et al. (2002). "Requirement of hippocampal CA3 NMDA receptors in associative memory recall". In: *Science* 297, pp. 211–218.
- Nakazawa, K. et al. (2003). "Hippocampal CA3 NMDA receptors are crucial for memory acquisition of one-time experience". In: *Neuron* 38, pp. 305–315.
- Oren, I. et al. (2006). "Synaptic currents in anatomically identified CA3 neurons during hippocampal gamma oscillations in vitro". In: *Journal of Neuroscience* 26, pp. 9923–9934.
- Patel, M. (2018a). "Effects of Adaptation on Discrimination of Whisker Deflection Velocity and Angular Direction in a Model of the Barrel Cortex". In: *Front Comput Neurosci* 12, pp. 45–60.
- (2018b). "Spiking and Excitatory/Inhibitory Input Dynamics of Barrel Cells in Response to Whisker Deflections of Varying Velocity and Angular Direction". In: *Neurosci* 369, pp. 15–28.
- (2019). "Analysis of Feedforward Mechanisms of Multiwhisker Receptive Field Generation in a Model of the Rat Barrel Cortex". In: *Journal of Theoretical Biology* 477, pp. 51–62.
- Patel, M. and B. Joshi (2013). "Decoding synchronized oscillations within the brain: phase-delayed inhibition provides a robust mechanism for creating a sharp synchrony filter". In: *J Theoretical Biol* 334, pp. 13–25.
- (2015). "Modeling the evolving oscillatory dynamics of the rat locus coeruleus through early infancy". In: *Brain Res* 1618, pp. 181–193.
- Patel, M., AV. Rangan, and D. Cai (2009). "A large-scale model of the locust antennal lobe". In: *Journal of Computational Neuroscience* 27, pp. 553–567.
- Patel, M., A.V. Rangan, and D. Cai (2013). "Coding of Odors by Temporal Binding within a Model Network of the Locust Antennal Lobe". In: *Frontiers in Comput Neurosci* 7.50, pp. 1–18.
- Patel, M. and M. Reed (2013). "Stimulus encoding within the barn owl optic tectum using gamma oscillations vs. spike rate: A modeling approach". In: *Network: Computation in Neural Systems* 24.2, pp. 52–74.
- Perez-Orive, J. et al. (2002). "Oscillations and sparsening of odor representations in the mushroom body". In: *Science* 297, pp. 359–365.

- Petersen, C. (2007). "The functional organization of the barrel cortex". In: *Neuron* 56.2, pp. 339–355.
- Petersen, C. and B. Sakmann (2000). "The excitatory neuronal network of rat layer 4 barrel cortex". In: *J Neurosci* 20, pp. 7579–7586.
- (2001). "Functionally independent columns of rat somatosensory barrel cortex revealed with voltage-sensitive dye imaging". In: *J Neurosci* 21, pp. 8435–8446.
- Pinto, D., J. Brumberg, and D. Simons (2000). "Circuit Dynamics and Coding Strategies in Rodent Somatosensory Cortex". In: *J Neurophysiol* 83.3, pp. 1158–1166.
- Pouille, F. and M. Scanziani (2001). "Enforcement of temporal fidelity in pyramidal cells by somatic feed-forward inhibition". In: *Science* 293, pp. 1159–1163.
- Puccini, G., A. Compte, and M. Maravall (2006). "Stimulus Dependence of Barrel Cortex Directional Selectivity". In: *PLoS One* 1, e137.
- Roy, N., T. Bessaih, and D. Contreras (2011). "Comprehensive mapping of whisker-evoked responses reveals broad, sharply tuned thalamocortical input to layer 4 of barrel cortex". In: *J Neurophysiol* 105, pp. 2421–2437.
- Rybak, IA. et al. (2004). "Modeling the ponto-medullary respiratory network". In: *Respir Physiol Neurobiol.* 143, pp. 307–319.
- Schubert, D., R. Kotter, and J. Staiger (2007). "Mapping functional connectivity in barrel-related columns reveals layer- and cell type-specific microcircuits". In: *Brain Struct Funct* 212, 107–119.
- Schubert, D. et al. (2003). "Cell type-specific circuits of cortical layer IV spiny neurons". In: *J Neurosci* 23, pp. 2961–2970.
- Sharp, T., R. Petersen, and S. Furber (2014). "Real-time million-synapse simulation of rat barrel cortex". In: *Frontiers in Neuroscience* 8, pp. 1–9.
- Shimegi, S. et al. (1999). "Temporal characteristics of response integration evoked by multiple whisker stimulations in the barrel cortex of rats". In: *J Neurosci* 19, pp. 10164–10175.
- Sik, A., N. Tamamaki, and TF. Freund (1993). "Complete axon arborization of a single CA3 pyramidal cell in the rat hippocampus, and its relationship with postsynaptic parvalbumin-containing interneurons". In: *Eur J Neurosci.* 5, pp. 1719–1728.
- Simons, D. (1985). "Temporal and spatial integration in the rat SI vibrissa cortex". In: *J Neurophysiol* 54, pp. 615–635.
- Simons, D. and G. Carvell (1989). "Thalamocortical response transformation in the rat vibrissa/barrel system". In: *J Neurophysiol* 61, pp. 311–330.

- Simons, D. and T. Woolsey (1984). "Morphology of Golgi-Cox impregnated barrel neurons in rat SmI cortex". In: *J Comp Neurol* 230, pp. 119–132.
- Sridharan, D., K. Boahen, and E.I. Knudsen (2011). "Space coding by gamma oscillations in the barn owl optic tectum". In: *J Neurophysiol* 105, pp. 2005–2017.
- Staiger, J. et al. (2009). "Local circuits targeting parvalbumin-containing interneurons in layer IV of rat barrel cortex". In: *Brain Struct Funct* 214, 1–13.
- Staiger, J. et al. (2016). "Morphological Characteristics of Electrophysiologically Characterized Layer Vb Pyramidal Cells in Rat Barrel Cortex". In: *PLOS One* 11, p. 10.
- Steriade, M. (2006). "Grouping of brain rhythms in corticothalamic systems". In: *Neuroscience* 137, pp. 1087–1106.
- Sun, Q., J. Huguenard, and D. Prince (2006). "Barrel Cortex Microcircuits: Thalamocortical Feed-forward Inhibition in Spiny Stellate Cells Is Mediated by a Small Number of Fast-Spiking Interneurons". In: *J Neurosci* 26.4, pp. 1219–1230.
- Swadlow, H. and A. Gusev (2002). "Receptive-field construction in cortical inhibitory interneurons". In: *Nat Neurosci* 5, pp. 403–404.
- Tao, L. et al. (2004). "An egalitarian network model for the emergence of simple and complex cells in visual cortex". In: *Proc Natl Acad Sci USA* 101, p. 366.
- Temereanca, S., E. Brown, and D. Simons (2008). "Rapid Changes in Thalamic Firing Synchrony during Repetitive Whisker Stimulation". In: *J Neurosci* 28, pp. 11153–11164.
- Temereanca, S. and D. Simons (2003). "Local field potentials and the encoding of whisker deflections by population firing synchrony in thalamic barreloids". In: *J Neurophysiol* 89, pp. 2137–2145.
- Thomson, A. et al. (2002). "Synaptic connections and small circuits involving excitatory and inhibitory neurons in layers 2-5 of adult rat and cat neocortex: triple intracellular recordings and biocytin labelling in vitro". In: *Cereb Cortex* 12, pp. 936–953.
- Tiesinga, P. and T. Sejnowski (2009). "Cortical enlightenment: Are attentional gamma oscillations driven by ING or PING?" In: *Neuron* 63, pp. 727–732.
- Timofeeva, E. et al. (2003). "A map of angular tuning preference in thalamic barreloids". In: *J Neurosci* 23, pp. 10717–10723.
- Timofeeva, E. et al. (2004). "Synthesis of multiwhisker-receptive fields in subcortical stations of the vibrissa system". In: *J Neurophysiol* 91, pp. 1510–1515.

- Traub, R. et al. (1996). "Analysis of gamma rhythms in the rat hippocampus in vitro and in vivo". In: *J Physiology* 493, pp. 471–484.
- Traub, R. et al. (2001). "Gap junctions between interneuron dendrites can enhance synchrony of gamma oscillations in distributed networks". In: *Journal of Neuroscience* 21, pp. 9478–9486.
- Wang, X. and G. Buzsaki (1996). "Gamma oscillation by synaptic inhibition in a hippocampal interneuronal network model". In: *J Neuroscience* 16, pp. 6402–6413.
- Wang, XJ. and J. Rinzel (1992). "Alternating and synchronous rhythms in reciprocally inhibitory model neurons". In: *Neural Computation* 4, pp. 84–97.
- Wehr, M. and A.M. Zador (2003). "Balanced inhibition underlies tuning and sharpens spike timing in auditory cortex". In: *Nature* 426, pp. 442–446.
- Welker, C. and T. Woolsey (1974). "Structure of layer IV in the somatosensory neocortex of the rat: description and comparison with the mouse". In: *J Comp Neurol* 158, pp. 437–453.
- Whittington, M., R. Traub, and J. Jefferys (1995). "Synchronized oscillations in interneuron networks driven by metabotropic glutamate receptor activation". In: *Nature* 373, pp. 612–615.
- Wilent, W. and D. Contreras (2005). "Dynamics of excitation and inhibition underlying stimulus selectivity in rat somatosensory cortex". In: *Nature Neuroscience* 8, pp. 1364–1370.
- Wilson, H and J. Cowan (1972). "Excitatory and inhibitory interactions in localized populations of model neurons". In: *Biophysical Journal* 12, pp. 1–24.
- Wilson, S. et al. (2010). "Modeling the Emergence of Whisker Direction Maps in Rat Barrel Cortex". In: *PLoS One* 5, e8778.
- Witter, MP. (2007). "Intrinsic and extrinsic wiring of CA3: indications for connectional heterogeneity". In: *Learn Mem.* 14, pp. 705–713.
- Wittner, L. et al. (2006). "Hippocampal CA3 pyramidal cells selectively innervate aspiny interneurons". In: *Eur J Neurosci.* 5, pp. 1286–1298.
- Zemankovics, R. et al. (2013). "Feedforward inhibition underlies the propagation of cholinergically induced gamma oscillations from hippocampal CA3 to CA1". In: *J Neurosci.* 33, pp. 12337–12351.
- Zhu, J. and B. Connors (1999). "Intrinsic firing patterns and whisker-evoked synaptic responses of neurons in the rat barrel cortex". In: *J Neurophysiol* 81, pp. 1171–1183.